Direct numerical simulation of free convection over a heated plate

Juan Pedro Mellado†

Max Planck Institute for Meteorology, Bundesstrasse 53, 20146 Hamburg, Germany

Direct numerical simulations of free convection over a smooth, heated plate are used to investigate unbounded, unsteady turbulent convection. Four different boundary conditions are considered: free-slip or no-slip walls, and constant buoyancy or constant buoyancy flux. It is first shown that, after the initial transient, the vertical structure agrees with observations in the atmospheric boundary layer and predictions from classical similarity theory. A quasi-steady inner layer and a self-preserving outer layer are clearly distinguished, with an overlap region between them of constant turbulent buoyancy flux. The extension of the overlap region reached in our simulations is more than 100 wall units $(\kappa^3/B_s)^{1/4}$, where B_s is the surface buoyancy flux and κ the corresponding molecular diffusivity (the Prandtl number is one). The buoyancy fluctuation inside the overlap region already exhibits the $-1/3$ power-law scaling with height for the four types of boundary conditions, as expected in the local, free-convection regime. However, the mean buoyancy gradient and the vertical velocity fluctuation are still evolving toward the corresponding power laws predicted by the similarity theory. The second major result is that the relation between the Nusselt and Rayleigh numbers agrees with that reported in Rayleigh–Bénard convection when the heated plate is interpreted as half a convection cell. The range of Rayleigh numbers covered in the simulations is then 5×10^7–10^9. Further analogies between the two problems indicate that knowledge can be transferred between steady Rayleigh–Bénard and unsteady convection. Last, we find that the inner scaling based on $\{B_s, \kappa\}$ reduces the effect of the boundary conditions to, mainly, the diffusive wall layer, the first 10 wall units. There, near the plate, free-slip conditions allow stronger mixing than no-slip ones, which results in 30 % less buoyancy difference between the surface and the overlap region and 30–40 % thinner diffusive sublayers. However, this local effect also entails one global, substantial effect: with an imposed buoyancy, free-slip systems develop a surface flux 60 % higher than that obtained with no-slip walls, which implies more intense turbulent fluctuations across the whole boundary layer and a faster growth.

Key words: convective boundary layer, geophysical flows, turbulent convection

---

† Email address for correspondence: juan-pedro.mellado@zmaw.de

1. Introduction

Turbulent free convection next to a horizontal interface is a common and important process in nature and engineering, whether it occurs due to variations in the fluid temperature, composition, or a combination thereof. It often appears in the form of a boundary layer, extending vertically over a length scale z_* which is much smaller than the horizontal one. It is expected that such a system develops an inner layer close enough to the surface in which z_*, the outer scale, drops out of the local scalings (Turner 1973; Monin & Yaglom 2007). This inner layer, also referred to as the surface layer, has been investigated within the context of the convective boundary layer that grows in the atmosphere under strongly unstable conditions, in which case z_* is commensurate with the height of a temperature inversion frequently capping the turbulence zone (Businger *et al.* 1971; Panosfky & Dutton 1984; Garratt 1992; Wyngaard 2010). It has also been studied within the scope of Rayleigh–Bénard convection, z_* then being the height of the convection cell (Townsend 1959; Belmonte, Tilgner & Libchaber 1994; Lui & Xia 1998; Fernandes & Adrian 2002; Maystrenko, Resagk & Thess 2007; du Puits *et al.* 2007; Reeuwijk, Jonker & Hanjalić 2008*b*). Some aspects of the problem were discussed by Prandtl (1932), who considered precisely the unbounded configuration studied in this paper.

However, both the fundamental understanding and the available data about the vertical structure in turbulent free convection are still incomplete, especially when compared to shear-driven wall-bounded turbulent flows (Tennekes & Lumley 1972; Pope 2000; Jimenez 2012). This last appreciation is arguably due at least in part to the physics of free convection, which might be intrinsically more complex because we have to cope with an active scalar and the details of the inner layer participate in shaping the forcing mechanism (Lohse & Xia 2010). Besides, considerable attention in Rayleigh–Bénard convection has been drawn to other relevant aspects of the problem, such as the functional relation between the Nusselt and Rayleigh numbers and the identification of different regimes (Siggia 1994; Grossmann & Lohse 2000; Ahlers, Grossmann & Lohse 2009; Stevens, Lohse & Verzicco 2011; He *et al.* 2012). Comparisons among the atmosphere, the laboratory and the simulations are further complicated by the observed strong dependence on the Rayleigh numbers and on the large-scale structures (du Puits *et al.* 2007; Reeuwijk, Jonker & Hanjalić 2008*a*; Bailon-Cuba, Emran & Schumacher 2010). Available data are also limited. In the laboratory, it is difficult to obtain accurate measurements inside that relatively thin inner layer, with simultaneous access to several quantities at several positions. In field campaigns, a controlled environment is unavailable and additional phenomena can complicate the problem significantly, e.g. moisture transport and cloud formation in the atmospheric boundary layer (Emanuel 1994; Stevens 2005; Weidauer, Pauluis & Schumacher 2010). Moreover, it is rare to find pure free convection and data are normally extrapolated from mixed convection (Businger 1973; Beljaars 1994; Grachev, Fairall & Bradley 2000). All this motivates our work, in which we use direct numerical simulations of temporally evolving turbulent free convection over a smooth, heated plate to analyse the structure of the flow, especially the inner layer, under controlled conditions.

One reason to consider the heated plate instead of the two conventional frameworks mentioned before is to extend that existing research with an unbounded configuration. Both Rayleigh–Bénard convection and the convective boundary layer constrain the vertical motion at a height z_*, with a rigid plate or with an inversion, respectively. In the former case, the aspect ratio is added as a second geometrical parameter. The removal of those length scales in the heated plate changes the large-scale structure

and thus the aforementioned interaction between this large-scale organization of the flow and the near-wall region. Analysis and comparison of systems with different large-scale structure can contribute to better understanding of its role inside the inner layer.

A second reason to consider the heated plate is the study of statistically unsteady convection and transient effects, important because there are many situations in which the external forcing changes frequently or varies continuously in time, e.g. a horizontal advection or the diurnal cycle. Therefore, this work complements again previous studies on Rayleigh–Bénard convection and on the developed stages of a convective boundary layer working against a stably stratified fluid, which are steady and quasi-steady problems, respectively. We refer to the latter as quasi-steady because the time rate of change of the height z_* is increasingly small compared to the velocity scale w_* of the turbulent fluctuations inside the convective boundary layer, namely, $(1/w_*)\, \mathrm{d}z_*/\mathrm{d}t \propto t^{-2/3}$ (e.g. Fedorovich, Conzemius & Mironov 2004); in contrast, in the heated plate, $\mathrm{d}z_*/\mathrm{d}t$ is always comparable to w_*.

It is also interesting to note that the configuration studied here corresponds to the convective boundary layer growing into a neutrally stratified fluid. Hence, on the one hand, this work provides reference data for the limit of small stratification in the more common case of free convection penetrating into a stably stratified fluid (Willis & Deardorff 1974; Deardorff, Willis & Stockton 1980; Fernando & Little 1990; Fedorovich *et al.* 2004; Sullivan & Patton 2011). On the other hand, it contributes to the understanding of transients of the convective boundary layer during which the background stratification is not yet felt by the turbulent motion. An example of this is the morning transition during which the residual layer is replaced by the new convective boundary layer (Garratt 1992; Wyngaard 2010). Despite the arguably short duration of these early stages, it is particularly interesting to investigate their surface layer because certain statistics therein tend toward a steady vertical structure in the developed phase, and therefore the initial properties of that layer might be representative of, and relevant to, the later-time behaviour.

Besides the characterization of the system in terms of basic properties such as buoyancy, velocity and vorticity, we also discuss the effect of the following boundary conditions: free-slip or no-slip for the velocity field, and constant buoyancy b_0 or constant buoyancy flux B_0 for the buoyancy field. Detailed work on this aspect of the problem is scarce, despite its relevance. For instance, in turbulent Rayleigh–Bénard convection, the role of the finite conductivity of the plates (Hunt *et al.* 2003; Verzicco 2004) and the differences between Dirichlet and Neumann boundary conditions for the active scalar (Verzicco & Sreenivasan 2008; Johnston & Doering 2009; Stevens *et al.* 2011) have been addressed only recently. Another example, this time in a geophysical context, is the air–water interface. Turbulent motion inside the atmosphere during the day experiences close to no-slip conditions at the bottom and approximately a constant temperature because of the higher heat capacity of the water. On the other hand, during the night, a combination between free- and no-slip conditions characterizes better the interface from the point of view of the sea-surface turbulent layer, along with a fixed flux imposed by radiative and/or evaporative cooling (Katsaros *et al.* 1977; Kraus & Businger 1994; Leighton, Smith & Handler 2003). Obviously, the above problems involve more phenomena than just free convection. Nevertheless, it is desirable to have a thorough understanding and characterization of simpler configurations, to be used as a reference; we provide one such reference in this paper.

Case	Velocity	Buoyancy	z_0	Grid	z_*^+	Ra_*	δ^+	c_{b2}
NsD	No-slip	b_0	$(\kappa^2/b_0)^{1/3}$	$3072 \times 3072 \times 1536$	298	1.8×10^9	4.2	1.18
FsD	Free-slip	b_0	$(\kappa^2/b_0)^{1/3}$	$2048 \times 2048 \times 1536$	329	1.7×10^9	3.0	1.17
NsN	No-slip	B_0	$(\kappa^3/B_0)^{1/4}$	$2048 \times 2048 \times 1536$	274	1.3×10^9	4.0	1.15
FsN	Free-slip	B_0	$(\kappa^3/B_0)^{1/4}$	$3072 \times 3072 \times 1536$	308	1.3×10^9	2.7	1.21

TABLE 1. Simulations. The second and third columns indicate the boundary conditions in the velocity, no-slip or free-slip, and in the buoyancy, Dirichlet (constant buoyancy b_0) or Neumann (constant buoyancy flux B_0). The corresponding length z_0 provides the remaining reference scales to non-dimensionalize the problem: $w_0 = \kappa/z_0$, a velocity; $t_0 = z_0^2/\kappa$, a time. $B_0 = w_0 b_0$ relates the parameters B_0 and b_0 in all cases. The convection length z_*^+, (3.5), the Rayleigh numbers Ra_*, (3.6), the gradient thicknesses δ, (3.11), and the power-law coefficients c_{b2}, (3.13), are given at the final time t_2.

The paper is organized as follows. In §2 we summarize the formulation and the set of simulations used in the analysis. Results are presented in §3. In §3.1 we define the vertical structure of the system, identifying outer and inner layers. In §3.2 we describe some major features of the outer layer; the remainder of the paper focuses on the inner layer. First, some properties at the wall are studied in §3.3 and the influence of the different boundary conditions on them are analysed in §3.4. Thereafter, the buoyancy, velocity and vorticity profiles are investigated in turn. Concluding remarks are presented in §4.

2. Formulation

The system is described in terms of the velocity vector $\boldsymbol{v}(\boldsymbol{x}, t)$, with components (v_1, v_2, w) along the directions Ox_1, Ox_2 and Oz, respectively, and the buoyancy $b(\boldsymbol{x}, t)$, equal to zero far enough above the plate. The evolution in time of these fields is determined by

$$\frac{\partial \boldsymbol{v}}{\partial t} + \boldsymbol{\nabla} \cdot (\boldsymbol{v} \otimes \boldsymbol{v}) = -\boldsymbol{\nabla} p + \nu \nabla^2 \boldsymbol{v} + b\boldsymbol{k}, \qquad (2.1a)$$

$$\boldsymbol{\nabla} \cdot \boldsymbol{v} = 0, \qquad (2.1b)$$

$$\frac{\partial b}{\partial t} + \boldsymbol{\nabla} \cdot (\boldsymbol{v}b) = \kappa \nabla^2 b. \qquad (2.1c)$$

The kinematic viscosity is ν, κ is the molecular diffusivity, p is a modified pressure divided by the reference density, and $\boldsymbol{k}$ is the unit vector along Oz. The system is statistically homogeneous inside the horizontal planes and the statistics depend on the distance z to the plate and time t.

The plate is rigid and impermeable ($w = 0$) and two boundary conditions are studied: no-slip ($v_i = 0$) and free-slip ($\partial v_i/\partial z = 0$). In terms of the buoyancy, two different forcings are considered: constant buoyancy at the wall ($b = b_0$ given) and constant surface buoyancy flux ($-\kappa \partial b/\partial z = B_0$ given). The set of configurations analysed in this work is summarized in table 1.

The initial velocity field is set to zero, and its mean value remains zero for all times. The initial condition for the buoyancy is

$$b(\boldsymbol{x}, 0) = b_i \left[1 - \mathrm{erf}\left(\frac{\sqrt{\pi}}{2} \frac{z}{\delta_i} \right) \right], \qquad (2.2)$$

where the buoyancy at the surface $b_i(x_1, x_2)$ and the thickness $\delta_i(x_1, x_2)$ are specified differently depending on the case. The local vertical buoyancy flux at the surface corresponding to this initial condition is $-\kappa \partial b/\partial z = \kappa b_i/\delta_i$. An initial broadband perturbation is defined by $\delta_i(x_1, x_2) = (\kappa b_0/B_0)(1 + \zeta(x_1, x_2))$, the random field ζ to be given. The case of constant buoyancy b_0 at the wall, corresponding to a Dirichlet boundary condition $b = b_0$, is obtained by setting $b_i(x_1, x_2) = b_0$. The case of constant surface flux B_0, corresponding to a Neumann boundary condition $\partial b/\partial z = -B_0/\kappa$, is obtained by setting $b_i(x_1, x_2) = b_0(1 + \zeta(x_1, x_2))$. The random field $\zeta(x_1, x_2)$ is characterized by a zero mean value and a Gaussian power spectral density centred at some given spatial frequency $1/\lambda$ and with a standard deviation equal to $1/(6\lambda)$, so that there is practically no energy with spatial frequencies below $1/(2\lambda)$. The phase of ζ is random.

The problem so defined depends on the parameters $\{\nu, \kappa, b_0\}$ or $\{\nu, \kappa, B_0\}$, according to the case, and the corresponding additional sets $\{\lambda, \zeta_{rms}, B_0\}$ or $\{\lambda, \zeta_{rms}, b_0\}$ characterizing the initial condition. Hence, the general solution can be expressed in non-dimensional form in terms of the Prandtl number $Pr = \nu/\kappa$ and non-dimensional parameters corresponding to the initial condition. In this work, the Prandtl number is set to 1 in all the cases and we study exclusively the fully developed turbulent regime that is established after the initial transient, once the initial conditions have been sufficiently forgotten. We will learn during the paper that some regions of the system become quasi-steady and others become self-similar inside this fully developed regime (Tennekes & Lumley 1972; Monin & Yaglom 2007). The initial condition (2.2) has been explained above in detail simply for completeness in the description of the simulations; further discussion can be found in the Appendix. Table 1 summarizes the corresponding reference scales constructed from the controlling parameters for each of the four configurations (Townsend 1959; Turner 1973).

High-order spectral-like compact finite differences are used to discretize (2.1) on a structured grid, along with a low-storage fourth-order accurate Runge–Kutta scheme to advance in time. The discrete solenoidal constraint is satisfied down to machine accuracy using a Fourier decomposition along the periodic horizontal planes x_1Ox_2 and a factorization of the resulting set of equations along the vertical coordinate (Mellado & Ansorge 2012). The top boundary of the computational domain is placed far enough from the turbulent region to avoid any significant interaction; no-penetration free-slip boundary conditions are used there, along with Neumann conditions for the scalar.

The reference grid size is $2048 \times 2048 \times 1534$, where the grid stretching in the vertical direction in the upper non-turbulent region leads to a height of the computational domain equal to $0.83L_0$, if $L_0 \times L_0$ is the horizontal size. The simulations are stopped when the boundary layer thickness is $\sim 0.3L_0$, to avoid finite-size effects on the results. It is argued in §1 that cases NsD and FsN (see table 1) are presumably the most interesting, since they are often used as an approximation (under certain conditions) to the air–water interaction at the common interface. Therefore, a larger domain $1.5L_0 \times 1.5L_0$ was considered in those two configurations to improve statistical convergence (i.e. $3072 \times 3072 \times 1534$). The reference Rayleigh number is $Ra_0 = b_0L_0^3/(\nu\kappa) = 3.6 \times 10^9$, or $Ra_0 = B_0L_0^4/(\nu\kappa^2) = 6.8 \times 10^{11}$, depending on the case. The thickness δ_i used in the initial condition (2.2) has a mean value $\kappa b_0/B_0 = 0.0053L_0$, which corresponds to ~ 11 mesh points. The random field ζ is defined by $\lambda/(\kappa b_0/B_0) = 4$ and the root-mean-square (r.m.s.) is $\zeta_{rms} = 0.1$. The resolution requirements and other aspects of the numerical solution are discussed in the Appendix.
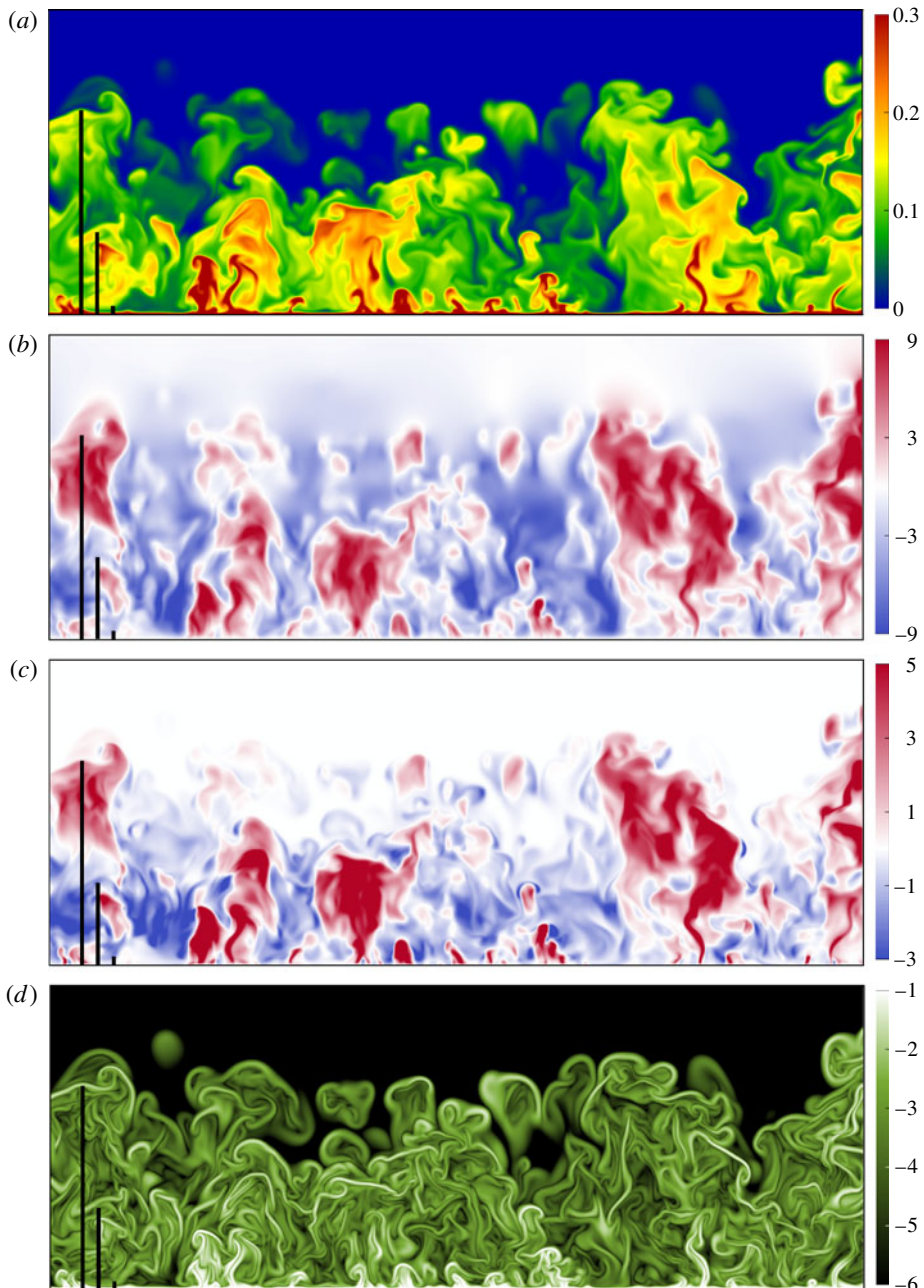
FIGURE 1. Visualization inside a vertical plane at the final time t_2: (*a*) scaled buoyancy b/b_s; (*b*) vertical velocity w^+; (*c*) vertical flux w^+b^+; (*d*) logarithm of the local dissipation rate $\log_{10} \epsilon_b^+$. The bars in the bottom-left corner indicate, from long to short: convection length z_*, (3.5); height of the inner layer, $0.4z_*$; thickness of the wall diffusive layer, 10 wall units.

3. Results

Figure 1 depicts the turbulent boundary layer inside a vertical plane in terms of the buoyancy b, the vertical velocity w, the vertical buoyancy flux wb and the local rate

of scalar dissipation $\epsilon_b = \kappa \, |\nabla b|^2$. The buoyancy varies between 0 far enough above the plate and b_0 at the plate itself, but a large part of that variation occurs in a very thin region next to the wall, the diffusive wall layer, and that is the reason to show only the range 0–$0.3b_0$ in figure 1(*a*), emphasizing thereby the morphology of the turbulence inside the bulk of the flow. Next to the wall, we observe the relatively small ascending plumes, shown in red. The upward motion of these structures is inferred from figure 1(*b*). These plumes extend approximately all across the inner layer and tend to merge into larger thermals as they rise, accelerating but becoming less buoyant as a result of the mixing with environmental fluid. (The exact definitions of the outer, inner and diffusive wall layers marked in that figure, as well as the normalization employed for the fields, will be provided in this section.)

Figures 1(*a*)–1(*c*) reveal unambiguously the structural similarity between the buoyancy and the vertical velocity fields, associating high values of buoyancy with ascending motions and thus an upwards buoyancy flux. Figures 1(*a*)–1(*c*) also reveal that intermittency characterizes the zone on top of the inner layer: turbulent thermals alternate with non-turbulent, unmixed fluid entrained from above (Pope 2000). This feature is illustrated even more clearly by the scalar dissipation rate in figure 1(*d*), where those regions of outer fluid are coloured in black and the turbulent/non-turbulent interface is defined more sharply. The typical lamellar structure of a scalar turbulent field is also readily observed in that last panel, with variations in ϵ_b of several orders of magnitude across relatively thin regions.

Figure 1 corresponds to case NsD in table 1, with no-slip boundary conditions and a constant buoyancy imposed at the surface. The other three cases considered in this study display a similar general structure, the only difference being the details of the region near the wall. As a function of time, the boundary layer simply thickens. In that mixing process, turbulence brings relatively cold fluid from above (shown in blue in figure 1*a*) near the hot plate below (red), and a dynamic balance is eventually achieved in which some mean properties within the inner layer become stationary. We focus on this fully developed turbulent regime.

3.1. *Buoyancy flux and vertical structure*

The vertical structure can be studied in terms of the mean buoyancy flux

$$B(z, t) = \langle b'w' \rangle - \kappa \, \partial \langle b \rangle / \partial z, \tag{3.1}$$

where angle brackets indicate horizontal averages and an apostrophe denotes a turbulent fluctuation. Both turbulent and molecular contributions are plotted in figure 2, normalized by the surface value

$$B_s(t) = B(0, t) = -\kappa \, \partial \langle b \rangle / \partial z(0, t). \tag{3.2}$$

The height z above the wall is measured in diffusion lengths – or wall units – by

$$z^+ = z \left(B_s / \kappa^3 \right)^{1/4}. \tag{3.3}$$

We follow in this way the notation commonly used for shear-driven wall-bounded turbulent flows (Tennekes & Lumley 1972; Pope 2000; Jimenez 2012). This normalization based on $\{B_s, \kappa\}$ constitutes the inner scaling and will be used throughout the paper (Townsend 1959; Fernandes & Adrian 2002). When the buoyancy flux at the wall B_s is fixed and equal to B_0, as occurs for cases FsN and NsN with Neumann boundary conditions for the buoyancy field, this set of scaling parameters is of course the same as that presented in table 1. On the other hand, if the mean
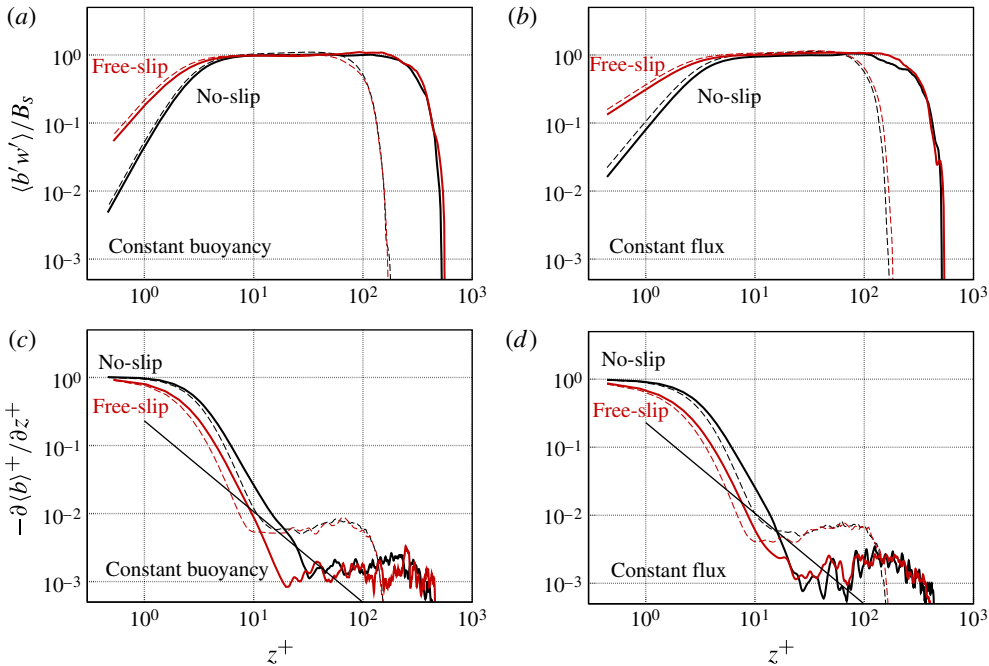
FIGURE 2. (Colour online) Profiles of the mean buoyancy flux: (a,b) turbulent contribution and (c,d) molecular contribution. (a,c) Cases NsD and FsD (Dirichlet, or constant buoyancy) and (b,d) cases NsN and FsN (Neumann, or constant buoyancy flux). Dashed line, early time $t_1^+ \simeq 50$; solid line, final time $t_2^+ \simeq 120$. The straight, solid line in (c,d) is $c_{b1}(z^+)^{-4/3}$ according to (3.14) using the value $c_{b1} = 0.23$ measured in the atmospheric boundary layer (Sorbjan 1996).

buoyancy at the surface

$$b_s(t) = \langle b \rangle (0, t) \qquad (3.4)$$

is fixed and equal to the control parameter b_0, as occurs in cases FsD and NsD with Dirichlet conditions, then $B_s(t)$ is not known *a priori* and it depends on the time t. However, we will learn below that this surface flux remains approximately constant after an initial transient, and the scales in table 1 still provide the correct order of magnitude. The inner velocity and buoyancy scales corresponding to the length scale $(\kappa^3/B_s)^{1/4}$ defined by (3.3) are $(B_s\kappa)^{1/4}$ and $(B_s^3/\kappa)^{1/4}$, respectively.

Several regions can be identified in figure 2 based on the relative contribution from molecular and turbulent transport to the total buoyancy flux, as sketched in figure 3 and now explained. Close enough to the wall, the molecular flux $-\kappa \partial \langle b \rangle / \partial z$ dominates. It decreases rapidly with height and becomes less than 1–5 % of the total flux at ∼10 wall units. We will refer to this relatively thin layer as the *diffusive wall region*, a term that, once more, has been borrowed from terminology used for shear-driven boundary layers. The observed width can be explained in terms of marginal stability (Townsend 1959) or using a surface strain model (Leighton *et al.* 2003). The diffusivity κ is important inside it.

A second region that is frequently differentiated next to the wall is the so-called *diffusive sublayer*, where the turbulent transport is still negligible compared to the
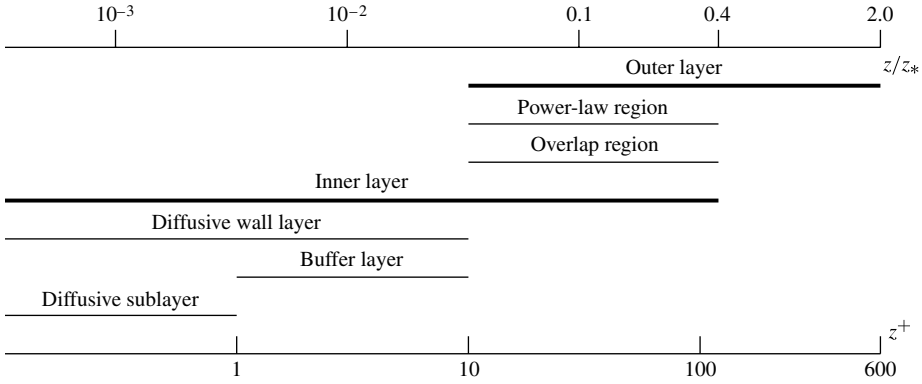
FIGURE 3. Vertical structure in free convection over a heated plate in terms of both outer variables z/z_*, with the convection length z_* defined by (3.5), and inner variables z^+, defined by (3.3); note the logarithmic scale. Simulations reach $z_*^+ \simeq 300$ at the final time t_2. This sketch follows that commonly used for the shear-driven boundary layer (Pope 2000).

molecular transport. For no-slip cases, figures 2(*a*) and 2(*b*) reveal that $\langle b'w' \rangle$ accounts for less than $\sim 10\%$ of the total flux for $z^+ < 1$, which suggests using this value as reference. Alternative definitions of this layer are also available in the literature and some of them will be used below explicitly. The remaining 90% of the diffusive wall region where both molecular and turbulent fluxes are important constitutes the *buffer layer*. It is also observed in figure 2(*a,b*) that free-slip systems have a larger turbulent contribution at $z^+ \simeq 1$. This dependence on the boundary conditions of the slope of $\langle b'w' \rangle$ next to the wall can be explained by the leading-order terms in the Taylor series expansion of the vertical velocity w and the buoyancy b around $z = 0$. The impermeability condition leads to the expansion $w' \propto z$, which further reduces to $w' \propto z^2$ for no-slip walls due to the solenoidal constraint at $z = 0$. Similarly, systems with a fixed surface buoyancy yield $b' \propto z$, and cases with an imposed buoyancy flux have a constant non-zero value $b' \propto b_{rms}$, to leading order. Hence, we obtain the following variations next to the wall for the four types of boundary condition in table 1: case NsD, $\langle b'w' \rangle \propto z^3$; case FsD, $\langle b'w' \rangle \propto z^2$; case NsN, $\langle b'w' \rangle \propto z^2$; case FsN, $\langle b'w' \rangle \propto z$. These power laws are precisely those observed in figure 2(*a,b*).

Outside of the diffusive wall region, beyond 10 wall units, we find the *outer layer*. This zone is characterized by the convection scale

$$z_*(t) = \frac{1}{B_s} \int \langle b'w' \rangle \, \mathrm{d}z, \qquad (3.5)$$

where the integral extends over the whole domain (Deardorff 1970, 1980; Fernandes & Adrian 2002). The evolution of the system can be discussed in terms of this length instead of the time. Indeed, the one-to-one correspondence between z_* and t allows us to replace the set $\{\kappa, B_s, z, t\}$ of independent variables by the set $\{\kappa, B_s, z, z_*\}$, for any statistic. Then, we can write this dependence non-dimensionally as $\{z^+, z_*^+\}$ or, equivalently, as $\{z/z_*, Ra_*\}$, where the convective Rayleigh number is defined by

$$Ra_*(t) = \frac{(2z_*)^3 \, 2b_s}{\nu \kappa} = (2z_*^+)^3 \, 2b_s^+, \qquad (3.6)$$
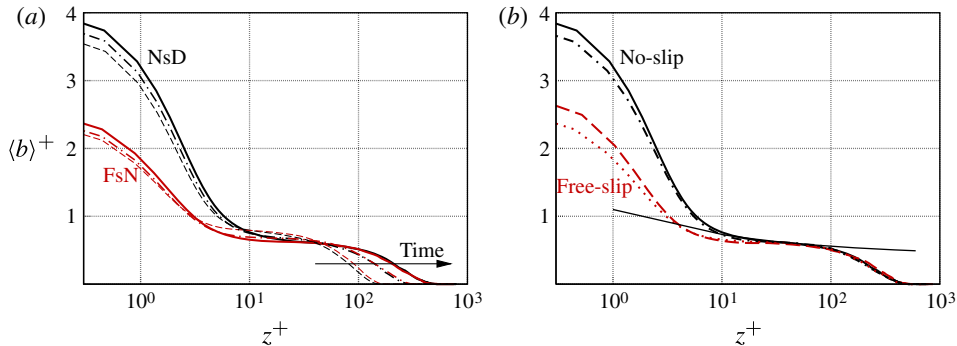
FIGURE 4. (Colour online) Profiles of the mean buoyancy. (*a*) The two cases NsD and FsN at different times: dashed line, $t_1^+ \simeq 50$; dot-dashed line, $t^+ \simeq 80$; solid line, $t_2^+ \simeq 120$. (*b*) Plot of all cases in table 1 at time t_2^+: solid line, case NsD; dashed line, case FsD; dot-dashed line, case NsN; dotted line, case FsN. The thin, solid line in (*b*) is the profile (3.15) using the values $c_{b1} = 0.23$ and $A = 1.1$.

having used the condition $Pr = 1$. (The factor of 2 in front of the length and the buoyancy is due to the interpretation of the heated plate as half of a convection cell, and will be explained more thoroughly in the next section.) By definition of the outer layer, the molecular diffusivity κ, and therefore Ra_*, drop out of the analysis inside that zone and $z/z_*(t)$ remains as the only independent variable. This outer scaling implies that the flow exhibits self-similarity as z_*, or equivalently Ra_*, increases with time. Further discussion is presented in § 3.2. In our simulations, this length scale grows from $z_*^+ \simeq 100$ at $t_1^+ \simeq 50$ to $z_*^+ \simeq 300$ at the final time $t_2^+ \simeq 120$. The Rayleigh number varies between $Ra_* \simeq 5 \times 10^7$ and $Ra_* \simeq 10^9$ in that same interval; final values are summarized in table 1. The outer velocity and buoyancy scales corresponding to the length scale z_* defined by (3.5) are $(B_s z_*)^{1/3}$ and $(B_s^2/z_*)^{1/3}$, respectively.

So far, the previous regions have been defined based on the relative turbulent and molecular contributions to the total buoyancy flux. In contrast, the inner layer is identified based on a quasi-steady behaviour developed in some of the statistics near the wall. For that purpose, let us consider the sum B of both molecular plus turbulent fluxes, (3.1). We can infer from figure 2 that B remains approximately constant over a large extent all the way down to the surface, that is,

$$\langle b'w'\rangle/B_s - \partial\langle b\rangle^+/\partial z^+ \simeq 1. \qquad (3.7)$$

The variation is less than 2 % in the no-slip cases and $\sim$6 % or less with free-slip walls. The main evolution of that region is simply a broadening – in our simulations, from $\sim$40 wall units at $t_1^+ \simeq 50$ to $\sim$120 at the final time $t_2^+ \simeq 120$. This result implies an approximately steady mean buoyancy $\langle b\rangle$ according to the transport equation $\partial\langle b\rangle/\partial t = -\partial B/\partial z$. This is corroborated in figure 4(*a*). The profiles in this figure show a relatively small 10 % variation close enough to the wall between the early and the last times, whereas the broadening of the boundary layer within that same interval of time is of the order of 200 %, from 100 to 300 wall units (note the logarithmic scale in the horizontal axis). Further, B_s is constant in the cases NsN and FsN, by definition, and B_s becomes constant, to leading order, in the configurations NsD and FsD. We have already anticipated this last behaviour in the beginning of this section and we will devote § 3.3 to its detailed analysis. Altogether, these observations suggest

that the term $z_*(t)$ containing the time dependence drops out of the set of independent variables $\{\kappa, B_s, z, z_*\}$ inside this region, and the first three variables allow us to write any functional relation in the form $f^+(z^+)$. This region is the so-called *inner* or *surface layer* and the expression $f^+(z^+)$ is the equivalent to the *law of the wall* in the shear-driven case (Tennekes & Lumley 1972; Pope 2000). In the heated plate, this inner layer extends to $\sim 0.4z^*$.

Finally, the area common to both the inner and outer layers is called the *overlap* or *inertial region* and it is characterized by a constant turbulent buoyancy flux approximately equal to B_s (see figure 2). Different scaling laws have been proposed in this region and some of them will be thoroughly explored later in §3.5. In particular, a power law for the mean buoyancy profile is predicted by similarity theory, which suggests using the name *power-law region* to refer to this zone in analogy to shear-driven configurations, where a *logarithmic-law region* is defined based on the corresponding functional form of the mean velocity profile.

The vertical structure discussed hitherto is summarized schematically in figure 3. Based on that structure, the system evolves as follows. As energy is introduced continuously through the surface, the turbulent boundary layer broadens in time and generates increasingly larger scales, but it does so keeping the near-wall structure approximately constant: figure 3 is only modified in that the end points of the inner and outer layers (thick lines) move to the right. Concomitantly, the overlap region thickens proportionally to z_*^+, the outer velocity scale $w_*^+ = (z_*^+)^{1/3}$ increases, the outer buoyancy scale $b_*^+ = (z_*^+)^{-1/3}$ decreases, the Rayleigh number defined in (3.6) grows proportionally to $(z_*^+)^3$, to leading order, and the outer-scale Reynolds number $w_*z_*/\nu = (z_*^+)^{4/3}$ increases too. The Kolmogorov length $\eta = (\nu^3/\varepsilon)^{1/4}$ remains approximately constant because of the inviscid scaling of the viscous dissipation rate $\varepsilon \simeq w_*^3/z_* = B_s$ (Tennekes & Lumley 1972). In fact, this latter relation indicates that the Kolmogorov length characterizing the small scales inside the turbulent region is comparable to the diffusion length z_0 characterizing the diffusive sublayer next to the wall (see table 1), which implies that the resolution requirements imposed by each of them are similar (see also Fedorovich & Shapiro 2009).

It is noted that, although the different regions have already been introduced in the literature for similar configurations, we provide here the specific defining heights for each of them. It is also worth observing that, in geophysical flows, the outer layer is usually not extended over the inner layer and an overlap region is not explicitly defined, so that only a local free-convection region as a part of the inner layer is considered in the discussion (Wyngaard, Coté & Izumi 1971; Garratt 1992). We have preferred here to follow the convention adopted in shear-driven flows on the basis that the investigation of parallelisms between the two driving mechanisms – velocity and buoyancy mean gradients – can provide further insight into each of them, and we need a common framework (Eckhardt, Grossmann & Lohse 2000, 2007). In this respect, it is also appropriate to comment on the fact that the logarithmic-law and the overlap regions in shear-driven systems do not coincide exactly with each other, the former being slightly broader than the latter (Pope 2000). The current simulations do not allow us to make an equivalent distinction between the power-law and the overlap regions in the heated plate, because of either limited statistical convergence or limited scale separation (moderate Reynolds and Rayleigh numbers).

3.2. *The outer layer*

We discuss briefly in this section some aspects of the outer layer before moving on to the analysis of the inner layer, which is the main focus of this paper. Apart from

the motivations explained in §1, another reason to concentrate on the inner layer is merely a technical one: the outer layer is characterized by intermittency and large-scale structures, and thus the statistical convergence there is less than it is closer to the wall (see the Appendix). Nonetheless, uncertainties of some properties relevant in geophysical flows are within 10–15 %, which is small enough to draw some interesting conclusions.

It is first observed that the definition of the outer scale z_* varies from author to author and from case to case. Here we follow Deardorff (1980) and use the integral definition (3.5) for two reasons. First, because of the neutral stratification in the fluid above the boundary layer there is no inversion with a more or less well-defined maximum mean buoyancy gradient or minimum turbulent buoyancy flux which can be used instead (Garratt 1992; Wyngaard 2010). Second, an integral definition is more robust than a pointwise one and it appears naturally in the integral analysis of the transport equations, as shown below. It is also observed that Deardorff (1980) uses a coefficient 2.5 in front of the integral and we do not. That is partly due to the shape of the buoyancy flux profile $\langle b'w' \rangle$, which has a triangular shape in the case of a convective boundary layer capped by an inversion while in the case of the heated plate the shape is more rectangular (recall figure 2). Moreover, visualizations in figure 1 support (3.5) and the discussion presented later in §3.3 favours this definition too.

The outer scaling described in §3.1 is confirmed in figure 5. This figure plots the r.m.s. $w_{rms} = \langle w^2 \rangle^{1/2}$ of the vertical velocity and the r.m.s. $v_{1,rms} = \langle v_1^2 \rangle^{1/2}$ of one of the two horizontal velocity components at different times (the symmetry of the problem implies $v_{1,rms} = v_{2,rms}$). When normalized with the outer, convective scales for the length z_* and velocity w_*, profiles at different times collapse on top of each other, that is, they become self-similar. This self-similar – or self-preserving – regime occurs in our simulations beyond $t^+ \simeq 80$. We will see below that inner-layer statistics approach their corresponding fully developed behaviour earlier in time, around $t^+ \simeq 50$. The reason is merely that the outer region involves longer time scales. The maximum vertical r.m.s. occurs at $\sim 0.4 z_*$, which coincides with the upper limit of the inner layer. The maximum of the horizontal r.m.s. is found closer to the wall or even at the wall itself (free-slip systems). Last, the variability of the profiles within the interval $z/z_* = 1$–2 also seen in figure 5 illustrates the limited statistical convergence already mentioned at the beginning of this section. That interval of heights corresponds precisely to the region of intermittency observed in figure 1.

Deardorff (1970) also proposed that the outer scales for the length z_*, the velocity w_* and the buoyancy b_* could be used to bring together data from different free-convection configurations, and not only for one individual problem at different times. This is indeed confirmed by figure 5 too, where the four different cases studied in this paper are plotted along with data reported in the cloud-top mixing layer. The latter is a relatively different system in which convection is driven by the evaporative cooling of the droplets at the horizontal cloud-top boundary in the presence of a strong, thin inversion (Mellado 2010). When the buoyancy difference across it is large enough, the inversion mimics the rigid plate in that it restricts the local vertical motion strongly and remains relatively flat. Then, a convective boundary layer develops downwards into the cloud, as in figure 1 but upside-down. The only difference from the plate is that the reference buoyancy flux B_0 is not imposed but results from a local equilibrium at the cloud top. However, once the appropriate reference buoyancy flux is identified, the two problems are alike, as proposed by Deardorff (1970): the collapse among the different curves in figure 5 is evident.
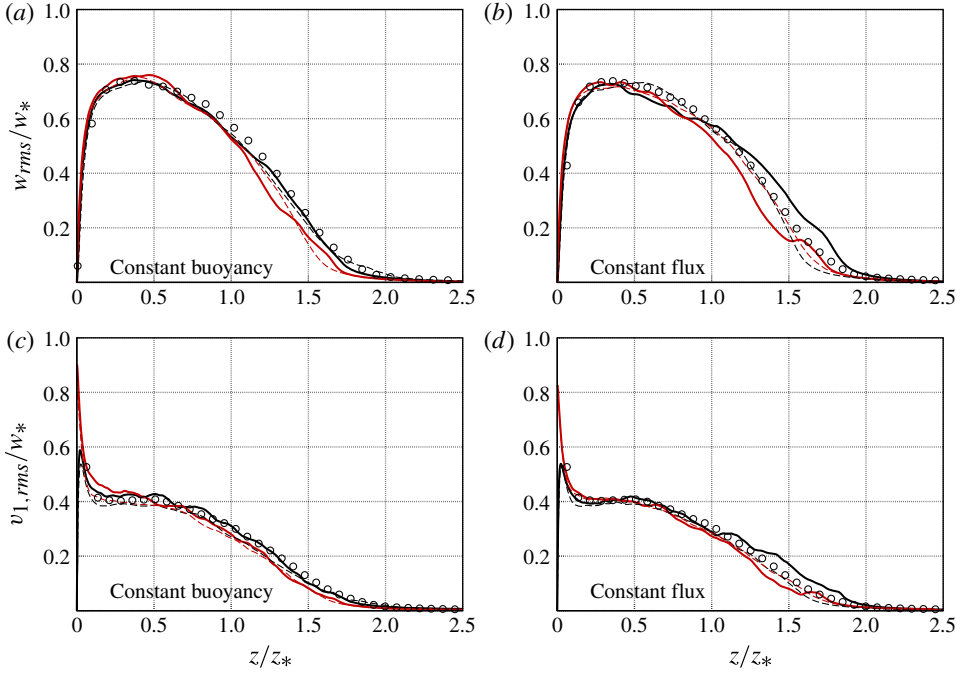
FIGURE 5. (Colour online) Profiles of the velocity r.m.s. using the outer (Deardorff) scaling: (*a,b*) vertical component and (*c,d*) horizontal component, (*a,c*) Cases NsD and FsD (Dirichlet, or constant buoyancy) and (*b,d*) cases NsN and FsN (Neumann, or constant buoyancy flux): dashed line, early time $t^+ \simeq 80$; solid line, final time $t_2^+ \simeq 120$. Red lines indicate free-slip conditions, black indicates no-slip walls. Symbols correspond to evaporatively driven free convection at the cloud top (Mellado 2010).

There are more analogies among those cases that further support the relevance of the outer scales in free convection. For instance, an explicit expression for the convection length $z_*(t)$ can be obtained from the analysis of the transport equation of the turbulence kinetic energy $k = (w_{rms}^2 + 2v_{1,rms}^2)/2$. The integral of this equation yields

$$\frac{\mathrm{d}}{\mathrm{d}t}(c_k z_* w_*^2) = (1 - c_\varepsilon)w_*^3, \qquad (3.8)$$

having introduced the non-dimensional coefficients

$$c_\varepsilon = \frac{1}{w_*^3}\int_0^\infty \varepsilon\,\mathrm{d}z, \quad c_k = \frac{1}{w_*^2 z_*}\int_0^\infty k\,\mathrm{d}z. \qquad (3.9)$$

In this expression, ε is the viscous dissipation rate. Details of the derivation can be found in Mellado (2010) and similar approaches have also been employed in the case of the convective boundary layer growing into a stratified fluid (Tennekes & Driedonks 1981; Zilitinkevich 1991; Fedorovich *et al.* 2004). In that case, the upper limit in the integrals above are set at the inversion height and certain assumptions are necessary regarding the turbulent transport term there, but the essence of the analysis is the same as here. The key point is that the coefficients (3.9) tend towards a constant value for a large enough Reynolds number. The ratio c_k does so because the convection scales w_* and z_* characterize the turbulent motion of the outer, convection layer and
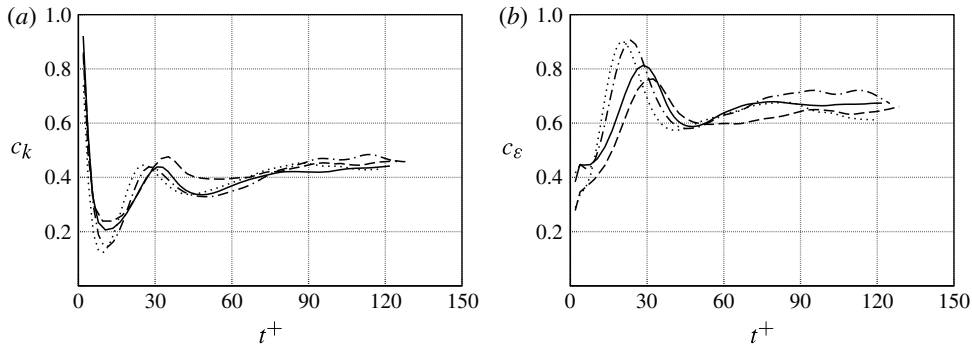
FIGURE 6. Temporal evolution of the parameters c_k and c_ε in the transport equation (3.8): solid line, case NsD; dashed line, case FsD; dot-dashed line, case NsN; dotted line, case FsN.

this layer accounts for almost all of the system at later times. Such a behaviour is observed in figure 6 beyond $t^+ \simeq 80$. The approximately steady evolution of c_ε after that initial transient, shown in figure 6(b), represents the inviscid scaling of the viscous dissipation rate (Tennekes & Lumley 1972).

Then, the assumption of constant coefficients and the identity $w_*^3 = B_s z_*$ leads to

$$\frac{\mathrm{d}z_*}{\mathrm{d}t} = f_2 w_*, \quad f_2 = 3(1 - c_\varepsilon)/(5c_k), \tag{3.10}$$

provided that B_s is constant or slowly varying. Similarly, we obtain explicitly the growth law $z_* \simeq [(2f_2/3)^3 B_s t^3]^{1/2}$. In principle, the growth-rate coefficient f_2 is of order one but could vary from case to case. However, this variability is relatively small and $f_2 \simeq 0.48$–0.54 is found in the cloud-top mixing layer while changing the controlling parameters by a factor of 2. We find $f_2 \simeq 0.4$–0.5 for the four configurations of the heated plate studied here. As occurred with the profiles in figure 5, the similarity of the numerical values of f_2 among different cases is striking.

These values of f_2 are larger than previous estimates derived from related configurations. Deardorff *et al.* (1980) estimated $f_2 \simeq 0.24$ from tank experiments. The values summarized in Tennekes & Driedonks (1981) based on field data are even lower, of the order of 0.14. There are several possible reasons for these differences, e.g. deviations from complete neutral conditions, the exact definition of z_* or the role of the horizontal wind. In this respect, direct numerical simulations can be used to clarify some of these aspects and set accurate reference values. Our results have reduced the uncertainty to $\sim$10–15 % in both coefficients c_k and c_ε, as observed in figure 6, and to $\sim$20 % in f_2. It is difficult to ascertain if this variability reflects a systematic dependence on the boundary conditions, or if it is just a consequence of the limited statistical convergence inside this outer region or the moderate Rayleigh numbers achieved in our simulations. Larger domains will answer this question in the future.

The remainder of the paper is devoted to the analysis of the inner layer.

3.3. *Wall values and dynamical balance*

The gradient thickness

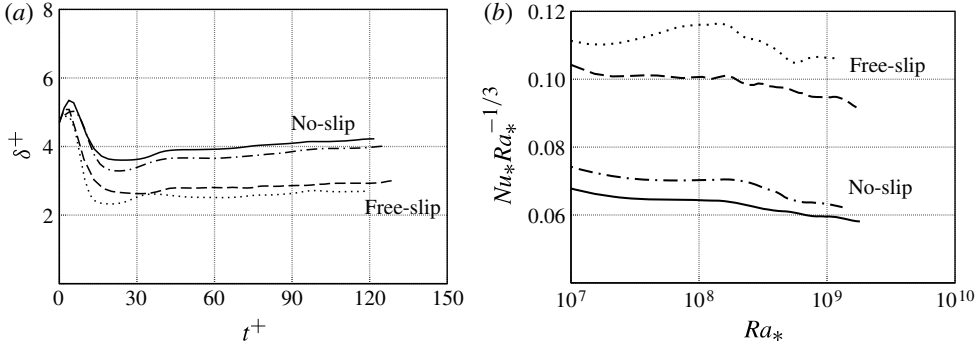$$\delta(t) = \frac{b_s}{B_s/\kappa} \tag{3.11}$$

FIGURE 7. Temporal evolution of (*a*) the gradient thickness δ, equation (3.11) and (*b*) the compensated Nusselt number as a function of the Rayleigh number: solid line, case NsD; dashed line, case FsD; dot-dashed line, case NsN; dotted line, case FsN.

introduced by Belmonte *et al.* (1994), where $b_s(t)$ is the mean buoyancy at the wall, defined in (3.4), and $B_s(t)/\kappa$ is the magnitude of the mean buoyancy gradient at the wall, defined in (3.2), proves useful in what follows. It is equal to the height at which the line tangent to $\langle b \rangle$ at the wall crosses the line $\langle b \rangle = 0$. From its definition and the inner scaling introduced in the §3.1, we obtain the identity $\delta^+ = b_s^+$, where $\delta^+(t) = \delta\,(B_s/\kappa^3)^{1/4}$ and $b_s^+(t) = b_s\,(\kappa/B_s^3)^{1/4}$. It is easy to show that $B_s/B_0 = (\delta/z_0)^{-1} = (\delta^+)^{-4/3}$ for cases NsD and FsD with an imposed buoyancy $b_s = b_0$, using thereby the (constant) parameters z_0 and b_0 from table 1 explicitly. For cases NsN and FsN with an imposed buoyancy flux $B_s = B_0$, this relation is equivalent to $b_s/b_0 = \delta/z_0 = \delta^+$. Therefore, all the information regarding those mean surface properties is contained in δ^+.

The temporal evolution of δ^+ is plotted in figure 7(*a*) and some important aspects of it are readily noticed. First, the values of order one confirm that the inner scaling is the appropriate one for δ. This result, in turn, indicates that this variable provides another measure of the diffusive-layer thickness, one often used in Rayleigh–Bénard convection (Belmonte *et al.* 1994; Lui & Xia 1998; Maystrenko *et al.* 2007; Stevens, Verzicco & Lohse 2010). Final values of δ^+ are collected in table 1. Second, figure 7(*a*) also shows that δ^+ remains approximately constant after the initial transient, between $t_1^+ \simeq 50$ and $t_2^+ \simeq 120$ (for comparison, z_* grows by a factor of 3 in that same interval of time). This steady behaviour quantifies the dynamical balance already mentioned in this section because of the equivalence between δ^+ and B_s in the Dirichlet cases NsD and FsD, and between δ^+ and b_s in the Neumann cases NsN and FsN: turbulence entrains outer fluid with low buoyancy and brings it close to the wall, where its buoyancy is increased, and it does so at that particular rate for the buoyancy and its flux at the surface to be constant, to leading order.

Quantitatively, the values of δ^+ obtained here for the heated plate agree with previous results from related configurations. For this comparison, it is appropriate to introduce the Nusselt number $Nu_* = B_s/(\kappa b_s/z_*) = z_*/\delta$ and to calculate the compensated Nusselt number $Nu_* Ra_*^{-1/3}$, which is related to the gradient thickness by $Nu_* Ra_*^{-1/3} = (2\delta^+)^{-4/3}$. This identity follows from the definition (3.6) and from the identity $\delta^+ = b_s^+$. In figure 7(*b*) we plot this compensated Nusselt number as a function of the Rayleigh number itself, as is customary in the study of Rayleigh–Bénard convection. It is then revealed that the data for no-slip walls vary between 0.06

and 0.07 within the interval $Ra_* \simeq 5 \times 10^7$–$10^9$ achieved in the present simulations. These values agree with measurements and simulations in Bénard cells (Siggia 1994; Ahlers *et al.* 2009; Stevens *et al.* 2011). The current results are also consistent with previous work in systems with free-slip conditions. Katsaros *et al.* (1977) measured $Nu\,Ra^{-1/3} \simeq 0.12$ for $Ra \simeq 10^9$ in tank experiments where convection was driven by the cooling at the air–water interface. Leighton *et al.* (2003) performed direct numerical simulations of this configuration at $Ra \simeq 10^7$ and obtained $\delta^+ \simeq 3.5$. More recently, Schumacher (2009) has reported compensated Nusselt numbers ~ 0.12 for $Ra \simeq 10^8$. All these values compare favourably with the data from the heated plate, indicating that turbulent free-slip systems increase the buoyancy transfer rate with respect to pure conduction more than no-slip configurations. This aspect of the problem is important and it is further discussed in § 3.4.

It is also worth noting at this point that the mild but monotonic increase of δ^+ with time depicted in figure 7(*a*) (equivalently, the decrease in the compensated Nusselt number in figure 7*b*) is equally a distinctive feature of Rayleigh–Bénard convection (Siggia 1994; Ahlers *et al.* 2009; Bailon-Cuba *et al.* 2010; Stevens *et al.* 2011). In agreement with these references, if a relation $Nu_* \propto Ra_*^\gamma$ is fitted to our data between $Ra_* = 5 \times 10^7$ and 10^9, values of the exponent γ are ~ 0.28–0.30 instead of $1/3$, closer to the result $\gamma = 2/7$ proposed by Castaign *et al.* (1989). Physically, this trend translates into a gentle but persistent modification of the dominant steady behaviour discussed so far: an increase in time of the buoyancy at the wall when the surface buoyancy flux is imposed, and a decrease in time of the flux when the buoyancy at the wall is fixed.

All these similarities between stationary Rayleigh–Bénard convection and unsteady convection indicate that properties from the former can be transferred to the latter, once the fully developed state is reached. These results also support the use of z_* as an outer scale, (3.5), and justifies the factor 2 in front of the length and the buoyancy scales used in the definition of the Rayleigh number, (3.6). The physical explanation for this factor is that the heated plate studied here can be interpreted as half the convection cell (Adrian 1996). In the former, the decrease of $\langle b \rangle$ with z from b_s at the wall towards $b = 0$ far from it occurs across a distance z_*. In the latter, $\langle b \rangle$ falls from the wall to the bulk value in the centre across half the cell height, and that bulk value is equal to half the buoyancy difference between the plates.

3.4. *Effect of the boundary conditions on the wall values*

In addition to the observed dynamical balance and the resulting analogy between unsteady and steady convection presented so far, another major aspect of the problem is the influence that different boundary conditions have on δ^+ (or, equivalently, on the compensated Nusselt number). With respect to the conditions imposed on the buoyancy field, the system forced with a constant buoyancy behaves similarly to that forced with a constant flux: $\sim 5\%$ variation for no-slip walls and $\sim 10\%$ for free-slip walls, according to figure 7(*a*) (see also table 1). In terms of the Nusselt number, figure 7(*b*), this means an increment of ~ 7 and 15%, respectively, when a constant surface flux is fixed. Notwithstanding the arguably small magnitude of this variation, this result differs from those reported in convection cells for similar Rayleigh numbers, where the sensitivity of the Nusselt number to this particular boundary condition is found to be negligible, at least for no-slip configurations (Johnston & Doering 2009; Stevens *et al.* 2011). The offset of $\sim 7\%$ observed here is quite robust through time and larger than uncertainties associated with the numerical simulation, which are shown in the Appendix to be less than 3%. It would be interesting to learn if those

discrepancies are a consequence of the different large-scale organization of the flow in the different configurations, and if they diminish as the Rayleigh number increases beyond the values attained in these simulations.

The effect of the boundary condition imposed on the velocity field is, on the other hand, remarkable. Free-slip conditions lead to 30 % smaller δ^+, approximately (see table 1), which translates into a larger Nusselt number by ∼60 % (see figure 7*b*). The same result is observed in convection cells: the Nusselt number reported by Schmitz & Tilgner (2009) for free-slip conditions is between 60 and 70 % larger than the same case with no-slip walls studied later by those same authors in Schmitz & Tilgner (2010) (see their reference case without rotation at $Ra = 10^7$ and $Pr = 7$). A similar increase of the rate of heat transfer is also observed by Julien, Legg & McWilliams (1996) in rapidly rotating configurations. This behaviour is similarly reported in earlier work, as reviewed by Katsaros *et al.* (1977).

Because of the relation $b_s^+ = \delta^+$, this dependence entails immediately a smaller normalised mean buoyancy at the surface for free-slip conditions. This is clearly shown in figure 4(*b*), where the mean profiles $\langle b \rangle$ at the final time t_2 are plotted: the inner scaling based on $\{B_s, \kappa\}$ collapses all the curves on top of each other inside the overlap region, but the effect of having free-slip conditions penetrates all across the diffusive wall layer, the first 10 wall units where the strong variation of $\langle b \rangle$ concentrates. Quantitatively, for cases with no-slip walls, the mean buoyancy drops from the surface value b_s to ∼0.18b_s at 15 wall units; for cases with free-slip conditions, that drop is less pronounced, from b_s to ∼0.25b_s.

This effect has important consequences. For a fixed surface flux B_0, it means that a significantly smaller mean buoyancy at the wall b_s will be measured with free-slip than with no-slip conditions, ∼30 % smaller (e.g. at the air–water interface: Katsaros *et al.* 1977; Leighton *et al.* 2003). This is consistent with the fact that free-slip systems do not restrict the horizontal motion at $z = 0$, which leads to stronger mixing next to the surface and thus to a more effective reduction of the mean buoyancy near the wall toward the far-field value. The measured gradient thickness δ is also ∼30 % smaller, which increases the resolution requirements to capture the corresponding structures.

Equivalently, for a fixed buoyancy b_0 at the wall, the higher turbulence intensity next to the surface with free-slip conditions increases the buoyancy transport in that region and eventually B_s itself. This is consistent with the smaller δ^+ observed for the configuration FsD compared to NsD and the relation $B_s/B_0 = (\delta^+)^{-4/3}$. The physical interpretation of the profiles in figure 4(*b*) in this situation, where we fix the buoyancy at the surface, is that the buoyancy inside the overlap region is ∼30 % higher in the case of free-slip walls (simply multiplying the two curves for cases NsD and FsD by $(B_s^3/\kappa)^{1/4}$ so that both share a common value $b = b_0$ at $z = 0$). The corresponding reduction of the thickness δ of the diffusion layer is ∼40 % and the increase in the measured flux B_s is 60 %. This last observation is very relevant: free-slip boundaries lead to a larger B_s, i.e. an increase of the rate at which energy is introduced into the system, which leads to a modification of global properties. In particular, from the scaling law $z_* \propto (B_s t^3)^{1/2}$ and the definitions $w_* = (B_s z_*)^{1/3}$ and $b_* = (B_s^2/z_*)^{1/3}$ discussed in §§ 3.1 and 3.2, it means a faster growth of the convective boundary layer and stronger fluctuations inside it for a given value of z_*, that is, for a given height of the turbulent region.

The effect of the velocity boundary condition on the near-wall structure underscored during the last paragraphs is portrayed in figure 8. The buoyancy field inside the plate at the final time t_2, as seen from above, is visualized there for the two systems
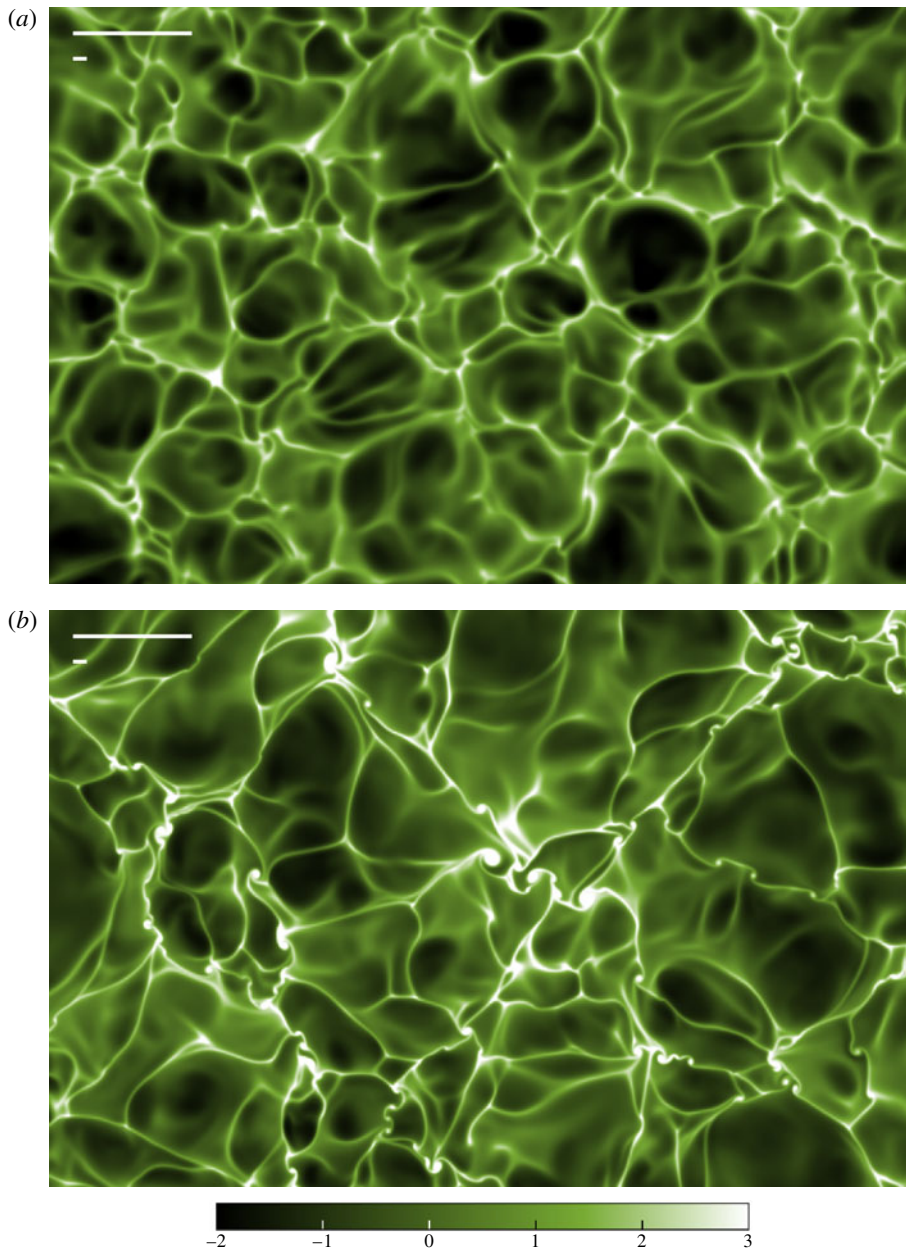
FIGURE 8. Normalized buoyancy $(b - \langle b \rangle)/b_{rms}$ inside a domain $3z_* \times 2z_*$ of the plate at the final time t_2: (*a*) no-slip conditions, case NsN; (*b*) free-slip conditions, case FsN. The white, longer bar in the top-left corner indicates the height of the inner layer, $0.4z_*$, and the shorter one indicates the thickness of the diffusive wall layer, 10 wall units.

NsN and FsN with an imposed flux B_0, the first one with no-slip walls and the second one with free-slip conditions. (The asymmetric range between $b_s - 2b_{rms}$ and $b_s + 3b_{rms}$ used in that figure is due to the positive skewness of the corresponding probability distribution function.) There are obvious similarities as well as some

differences between the two cases. As similarities, both cases reproduce coherent structures common to free convection: we observe cells of relatively low buoyancy fluid associated with descending currents and convergence lines of higher buoyancy defining the boundary of those cells. From the reference bars included in the figure, we infer that the typical diameter of the cells is comparable to the height of the inner layer, $\sim 0.4 z_*$. We can also infer that the typical width of the convergence lines is a few wall units, a fraction of the diffusive wall layer and thus comparable to δ, the gradient thickness (Asaeda & Watanabe 1989; Theerthan & Arakeri 2000; Flack, Saylor & Smith 2001; Shishkina & Wagner 2008). The convergence lines constitute the base of sheet-like updraft motion transporting relatively high buoyancy fluid, the plumes identified in figure 1. Visualizations at different heights within the diffusive wall layer (not shown) also indicate the formation of mushroom-like plumes as those sheet-like plumes collide with each other, in agreement with recent analysis in Rayleigh–Bénard convection (Shishkina & Wagner 2006; Zhou, Sun & Xia 2007; Shishkina & Wagner 2008; Schumacher 2008, 2009). The same morphology (convergence bands, updraft curtains, dust devils) has often been observed in the atmospheric boundary layer (Stull 1988).

However, there are also differences between figures 8(*a*) and 8(*b*). In free-slip systems, there exists a tendency to thinner sheet-like plumes between the convective cells and a enhanced vorticity inside the mushroom-like plumes at the nodal points of the cellular network. This observation is consistent with the formation of stronger horizontal near-wall currents, a recurrent argument throughout the paper that helps to explain several features: thinner convergence lines as those currents collide with each other; faster horizontal jet-like velocities along them and thereby stronger vertical vorticity; enhanced mushroom-like plumes in the convergence nodes; faster ascent currents inside the plumes. Eventually, it also explains the larger values of the Nusselt number, since the plumes are responsible for a large amount of the transport of buoyancy away from the plate (Shishkina & Wagner 2008). This phenomenology is supported by the buoyancy, velocity and vorticity r.m.s. profiles discussed in the following sections.

3.5. *Buoyancy profiles*

The vertical variation of the buoyancy r.m.s. $b_{rms} = \langle b'^2 \rangle^{1/2}$ in cases NsD and FsD with an imposed buoyancy b_0 at the wall, presented in figure 9(*a*), is characterized by a conspicuous maximum within the diffusive wall layer followed by a monotonic decrease, first smoothly across the inner layer and then more abruptly across the remaining part of the outer layer. The location of that maximum remains approximately constant in time at a height δ_{rms} comparable to, though smaller than, the gradient thickness δ, as shown in figure 10(*a*). This relation agrees with results from Rayleigh–Bénard convection (Townsend 1959; Belmonte *et al.* 1994; Maystrenko *et al.* 2007; Stevens *et al.* 2010), although differences by a factor of two have also been reported (du Puits *et al.* 2007). On the other hand, the near-wall structure is very different if a surface buoyancy flux B_0 is imposed: figure 9(*b*) reveals that the whole diffusive sublayer contains buoyancy fluctuations, in spite of molecular transport dominating the system in that narrow region. There exists a slight maximum at ~ 2–3 wall units, also observed by Leighton *et al.* (2003) beneath an air–water interface and by Stevens *et al.* (2011) next to a no-slip wall, but the relative variation in b_{rms} is only 2–3 %, which is comparable to the uncertainty due to finite size effects and statistical convergence in our simulations, and therefore inconclusive.
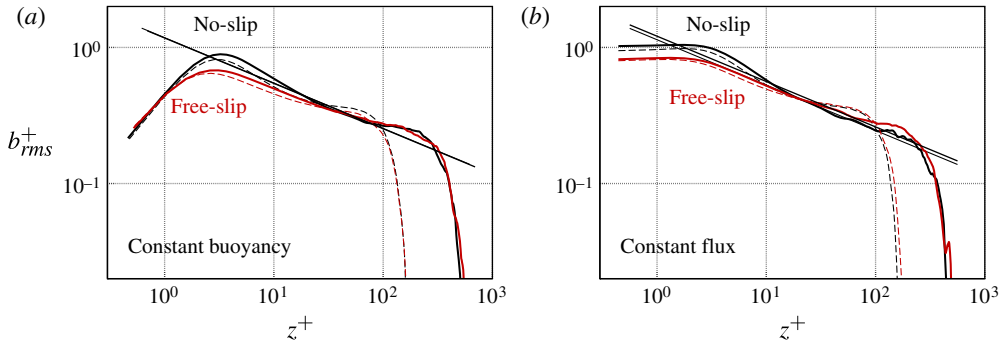
FIGURE 9. (Colour online) Profiles of buoyancy r.m.s. (*a*) Cases NsD and FsD (Dirichlet, or constant buoyancy) and (*b*) cases NsN and FsN (Neumann, or constant buoyancy flux): dashed line, early time $t_1^+ \simeq 50$; solid line, final time $t_2^+ \simeq 120$. The straight, solid line is $c_{b2} (z^+)^{-1/3}$ according to (3.13) using the values c_{b2} shown in table 1.
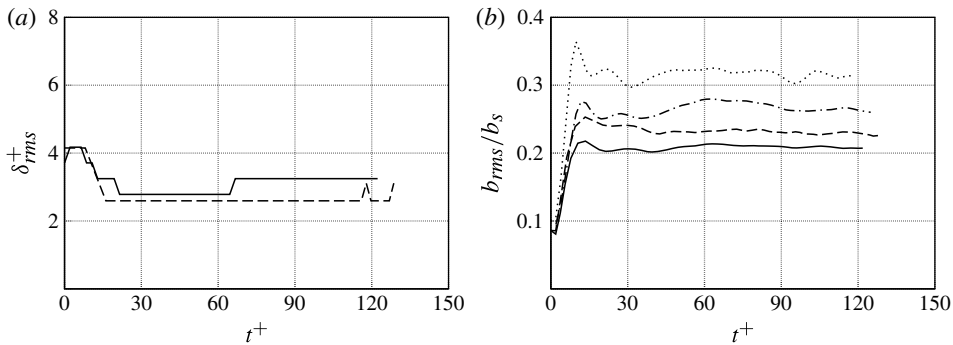

FIGURE 10. Temporal evolution of (*a*) the height of the maximum buoyancy r.m.s. and (*b*) the magnitude itself normalized by the mean surface value: solid line, case NsD; dashed line, case FsD; dot-dashed line, case NsN; dotted line, case FsN.

The temporal evolution of the maximum buoyancy fluctuation normalized with the mean surface buoyancy b_s, plotted in figure 10(*b*), tends to a constant between 0.2 and 0.3, depending on the boundary conditions. These turbulence intensities, in particular the value 0.2 with no-slip walls, are comparable to those obtained in Bénard cells, which vary between 0.1 and 0.2 (Belmonte *et al.* 1994; Maystrenko *et al.* 2007; du Puits *et al.* 2007; Verzicco & Sreenivasan 2008). (Recall that b_s in the current system is equivalent to half the buoyancy difference between the plates in the convection cell, and a factor of 2 needs to be taken into account when comparing this statistic between the two configurations.) It is also seen that forcing the system with a constant flux leads to intensities 30–40 % higher than those obtained with a constant buoyancy, consistent with the fact that those profiles need not fall to zero at the wall. In particular, the values in the interval 0.26–0.28 obtained here with no-slip conditions agree with the results obtained in convection inside a cylinder (Verzicco & Sreenivasan 2008; Stevens *et al.* 2011).

We now turn to the discussion of the overlap region between the inner and outer layers, which approximately corresponds to $10 < z^+ < 120$ in our simulations at the

final time t_2. Similarity theory predicts that molecular properties drop out from the set of independent variables $\{\kappa, B_s, z\}$ characterizing the inner layer, and some statistics can be expressed solely in terms of B_s and z (Prandtl 1932; Obukhov 1946; Priestley 1954). This hypothesis leads to the introduction of the local, free-convection scales

$$w_f(z) = (B_s z)^{1/3}, \quad b_f(z) = (B_s^2/z)^{1/3}, \tag{3.12}$$

which may be applied to normalize different statistics (Wyngaard *et al.* 1971; Garratt 1992).

In terms of the buoyancy fluctuation, this theory yields

$$b_{rms} = c_{b2} b_f = c_{b2} (B_s^2/z)^{1/3}, \tag{3.13}$$

where c_{b2} is a constant of order one. It is confirmed by figure 9. A curve $b_{rms}^+ = c_{b2} (z^+)^{-1/3}$ has been fitted in the range $10 < z^+ < 120$ at the final times, and the values of the coefficient c_{b2} for the different cases are included in table 1. They are indeed of order one for all the boundary conditions, the observed interval 1.1–1.2 agreeing reasonably well with the range 1.3–1.4 reported in the literature (Wyngaard *et al.* 1971; Stull 1988).

The power law $b_{rms} \propto z^{-\beta}$, however, has often been a matter of debate. A faster decay rate was documented in early work on Rayleigh–Bénard convection, with exponents β varying between 0.6 and 0.8 instead of $1/3$ (Townsend 1959; Belmonte *et al.* 1994). Thus, alternative scalings have been proposed, in particular $\beta = 1/2$ and logarithmic relations (Adrian 1996; Fernandes & Adrian 2002); we do not find any of these scalings. Plausible causes for this dispersion of results are the influence of the large-scale coherent motions imposed by a specific geometry and Rayleigh number effects. The former explanation was considered by Belmonte *et al.* (1994) and has been confirmed more recently by Maystrenko *et al.* (2007), who observe a 20 % variation in β for $Ra \simeq 10^7$ depending on the position in their rectangular cell where the measurements were taken. Similarly, du Puits *et al.* (2007) find a non-monotonic variation in β of $\sim 25\%$ as they change the aspect ratio from 1 to 10 in their cylindrical cell, but unfortunately the Rayleigh number is not kept constant in this set of experiments. Regarding the dependence on the Rayleigh number, Maystrenko *et al.* (2007) report a strong one, with β decreasing from 0.63–0.77 at $Ra \simeq 5 \times 10^7$ to $\beta \simeq 0.43$–0.44 at $Ra \simeq 6 \times 10^8$, closer to the theoretical prediction $\beta = 1/3$. Du Puits *et al.* (2007) observe even smaller values, between 0.30 and 0.47, for higher Rayleigh numbers, between 10^9 and 10^{11}. This behaviour suggests that the overlap region where the classical similarity theory applies might not be broad enough for the moderate Rayleigh numbers considered in the early work. Our results support this interpretation. Figure 2(*a,b*) indicates that the overlap region extends approximately between 10 and 40 wall units at t_1, when $Ra_* \simeq 5 \times 10^7$. This is certainly too thin a region, still comparable in size with the diffusive wall layer. Consequently, the profiles in figure 9, in particular those corresponding to the cases with no-slip boundary conditions, do not yet show a well-established power law at that early time. Actually, a variation close to $z^{-1/2}$ could be proposed between the maximum b_{rms} and 10 wall units, but this would be inappropriate because that zone still belongs to the diffusive wall layer and not to the overlap region. For later times t_2, for which $Ra_* > 10^9$, the overlap region is broader and then the exponent $\beta = 1/3$ is observed.

In contrast to the buoyancy fluctuation discussed so far, the local, free-convection scaling (3.12) is not yet established in the mean buoyancy profiles. This scaling can be

written in terms of the derivative (e.g. Garratt 1992) as

$$\frac{z}{b_f}\frac{\partial \langle b \rangle}{\partial z} = -c_{b1}, \qquad (3.14)$$

which implies $\partial \langle b \rangle^+/\partial z^+ = -c_{b1}(z^+)^{-4/3}$ or the equivalent expression for the mean buoyancy itself,

$$\langle b \rangle^+ = A + 3c_{b1}[(z^+)^{-\alpha} - 1], \qquad (3.15)$$

with $\alpha = 1/3$ and A a constant of integration. Relation (3.14) is included in figure 2(c,d) using the value $c_{b1} = 0.23$ estimated by Sorbjan (1996) from the atmospheric data corresponding to the 1968 Kansas field program (Businger *et al.* 1971; Wyngaard *et al.* 1971). The profile (3.15) is included in figure 4(b), having used a value $A = 1.1$. It is seen that the order of magnitude obtained from the simulations inside the first half of the overlap region compares favourably with that of the measurements, and there is certain tendency towards the result from similarity theory, but it is equally observed, particularly in figure 2(c,d), that a clear power law does not yet exist.

This difficulty in obtaining a well-defined scaling in the mean buoyancy is also shared in laboratory and field observations. A thorough review of laboratory measurements of the exponent α is provided by du Puits *et al.* (2007). Early work by Townsend (1959) favoured $\alpha = 1$ according to the Malkus theory instead of $\alpha = 1/3$ according to the similarity theory. More recently, measurements closer to $\alpha = 1/2$ have been reported (Maystrenko *et al.* 2007; du Puits *et al.* 2007), but these values were probably obtained within the buffer layer and not within the overlap region. Following the discussion above about the r.m.s., one possible explanation for this difficulty is that the overlap region is still too shallow and higher Rayleigh numbers are necessary, apparently higher for $\langle b \rangle$ than for b_{rms}. Nevertheless, in atmospheric research, where the Rayleigh numbers are much higher, available data for the exponent α are also scattered between 1/3 and 1/2 (Businger *et al.* 1971; Grachev *et al.* 2000). In this geophysical context, the variability has been attributed to the difficulty of having pure free convection, in addition to the sensitivity to the mean shear next to the surface being stronger in the mean profiles $\langle b \rangle$ than in the fluctuation profiles b_{rms} (Businger 1973). Another possible explanation might be that the outer scales have a weak influence on the r.m.s. but a strong one in the mean gradient. In this respect, it is worth noting that such an interaction between the inner and outer layers is observed not only in free convection, but also in shear-driven wall-bounded flows (Jimenez 2012). Direct numerical simulations, where controlled conditions are possible, are clearly advantageous in this respect, and future work with larger computational domains, and therefore a broader overlap region, could address this issue.

3.6. *Velocity profiles*

Some aspects of the velocity field have already been discussed in §3.2 using the outer scaling (see also figure 1b). In this section, we analyse the r.m.s. profiles of the vertical and the horizontal components using the inner scaling. The vertical r.m.s. $w_{rms} = \langle w^2 \rangle^{1/2}$, plotted in figure 11(a,b), is zero at the boundary because of the no-penetration condition and increases within the diffusion sublayer according to the Taylor expansions $w_{rms} \propto z^2$ in the no-slip cases NsD and NsN and $w_{rms} \propto z$ in the free-slip cases FsD and FsN. At ~ 10 wall units, the profiles incline towards the power
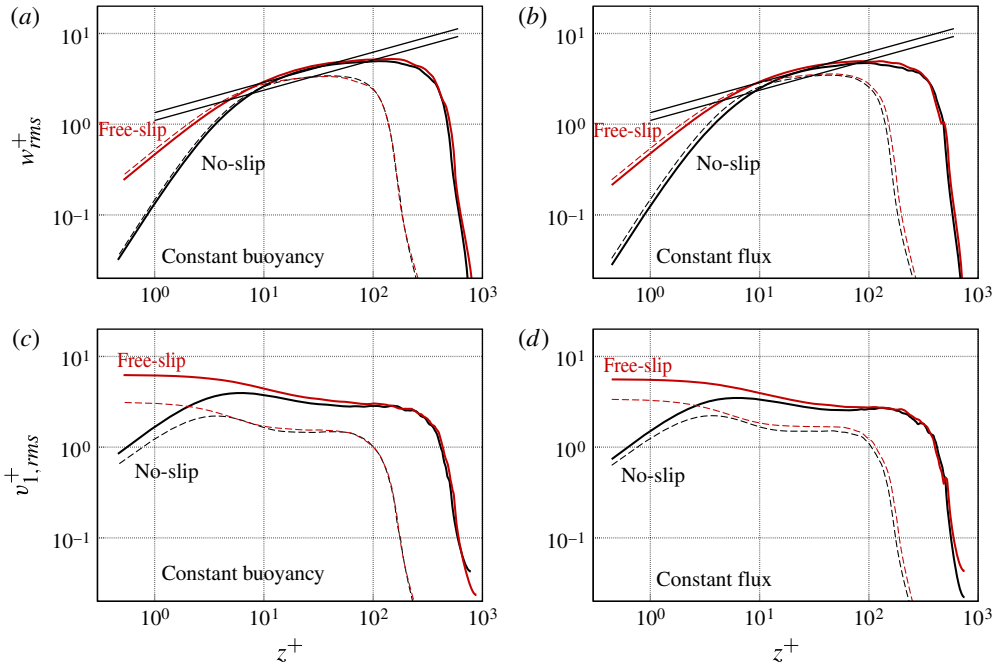
FIGURE 11. (Colour online) Profiles of the velocity r.m.s.: (a,b) vertical component and (c,d) horizontal component. (a,c) Cases NsD and FsD (Dirichlet, or constant buoyancy) and (b,d) cases NsN and FsN (Neumann, or constant buoyancy flux): dashed line, early time $t_1^+ \simeq 50$; solid line, final time $t_2^+ \simeq 120$. The straight, solid line in (a,b) is $c_{w2}(z^+)^{1/3}$ according to (3.16) using the interval of values c_{w2} measured in the atmospheric boundary layer (Wyngaard *et al.* 1971; Stull 1988).

law

$$w_{rms} = c_{w2}w_f = c_{w2}(B_s z)^{1/3} \tag{3.16}$$

predicted by the similarity theory for the overlap region. However, despite an incipient trend towards this scaling, a clear $1/3$ power law is not yet established for the Rayleigh numbers achieved in these simulations, of the order of 10^9. This is somewhat surprising because we have learnt before that $\langle b'w' \rangle$ is constant inside that layer and that $b_{rms} \propto z^{-1/3}$: it implies that the correlation coefficient between b and w is still changing with height. Nonetheless, the prediction (3.16) has been included in figure 11(a,b) using the interval $c_{w2} = 1.1$–1.34 reported in atmospheric measurements (Wyngaard *et al.* 1971; Stull 1988), and it shows certain agreement with the data from the simulations, especially with no-slip walls. Alternative scalings have been tested as was done for the buoyancy field, in particular $w_{rms} \propto \ln z$ (Fernandes & Adrian 2002), but also without success.

With respect to the temporal evolution of w_{rms}, the maximum value continuously increases and its location moves farther away from the surface as the boundary layer broadens, since both properties are proportional to the outer scales w_* and z_*, respectively (recall figure 5a,b). On the other hand, for a fixed height z inside the overlap region, w_{rms} asymptotes to a constant as the system evolves in time, as occurred with the buoyancy statistics discussed in the previous sections.

In contrast, the horizontal fluctuations do not become steady next to the wall. This is shown unequivocally in figure 11(*c,d*) plotting the r.m.s. $v_{1,rms} = \langle v_1^2 \rangle^{1/2}$ of the velocity component along the Ox_1 direction. The peak occurs at the plate for free-slip conditions and increases monotonically in time. With no-slip conditions, that growing maximum is off the plate and moving upwards, but still inside the diffusive wall region at $Ra_* \simeq 10^9$. In fact, figure 5(*c,d*) suggests that $v_{1,rms}$ scales inside the inner region with the outer, convective velocity $w_*(t)$ instead of doing it with the local, free-convection scale $w_f(z)$, in agreement with observations in atmospheric flows at much larger Rayleigh numbers (Panofsky *et al.* 1977; Garratt 1992). The implication of this time dependence is that outer-scale characteristics penetrate all across the system down to the surface, as already noted in the previous section. Another prominent signature of the large-scale, coherent structures inside the near-wall region is the cellular pattern at the surface itself seen in figure 8, the diameter of those cells being comparable to the inner-layer height. This behaviour is remarkable because similarity theory assumes precisely that z_* is irrelevant inside the inner layer: some statistics seem to follow that assumption well enough for the corresponding scalings to be obtained, whereas some other statistics react more strongly to the outer variables.

In terms of the effect of the boundary conditions, the velocity statistics corroborate the main conclusions drawn before from the study of the buoyancy statistics. First, the normalization with inner variables restricts the differences to the near-wall region. Surface properties penetrate into the overlap region slightly deeper in the velocity field than in the buoyancy, as inferred from the comparison of figure 11 with figure 9. Second, with respect to the boundary conditions for the buoyancy field, the difference between forcing the system with constant buoyancy or constant flux is minor: the latter leads to $\sim 10\%$ smaller intensities in the horizontal fluctuation and there is no significant effect in the vertical fluctuation. Third and most important, boundary conditions for the velocity field modify the near-wall region markedly: free-slip systems have stronger velocity fluctuations and thus more intense mixing in that zone, as noted earlier while discussing the gradient thickness δ, the planform structure in figure 8 and the turbulent fluctuation b_{rms}. This is most evident in the horizontal component, figure 11(*c,d*), which attains its maximum precisely at the surface. In the case of the vertical component, figure 11(*a,b*), the difference is also maximum within the diffusive sublayer because w grows proportionally to z instead of z^2 with free-slip walls, and thus we find there values of w_{rms} up to 4–6 times larger than in the no-slip case. This difference decreases to $\sim 8\%$ in the lower part of the outer layer, at ~ 20 wall units in our simulations, and beyond that distance both curves tend to collapse on top of each other; similar behaviour is observed in $v_{1,rms}$.

3.7. *Vorticity profiles*

The last property discussed in this paper is the vorticity, interesting because it emphasizes the differences in the near-wall region between free- and no-slip boundary conditions and because it provides insight into the local kinematics of the flow. The vorticity, like the velocity earlier, is discussed in terms of the r.m.s. $\omega_{z,rms} = \langle \omega_z^2 \rangle^{1/2}$ of the vertical component and the r.m.s. $\omega_{1,rms} = \langle \omega_1^2 \rangle^{1/2}$ of the horizontal component along the Ox_1 direction (the symmetry of the problem implies $\omega_{1,rms} = \omega_{2,rms}$). Their profiles are presented in figure 12.

Similarly to the velocity, the effect of having constant buoyancy or constant flux as boundary condition is negligible compared to the influence of having free- or no-slip walls. This influence is predominantly restricted to the diffusive wall layer, and the curves collapse on top of each other far enough above the plate when normalized
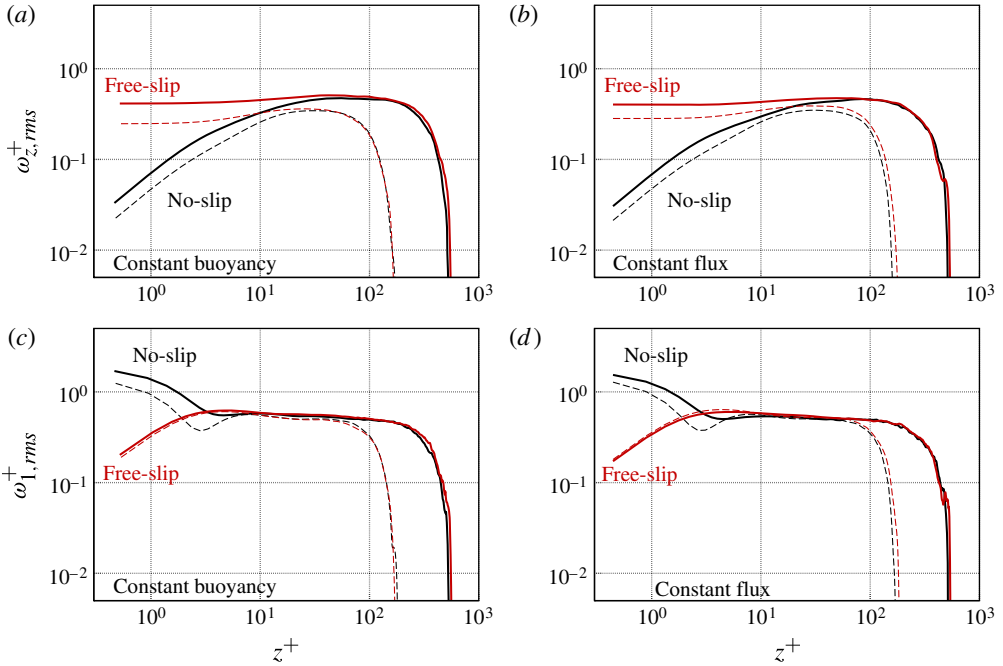
FIGURE 12. (Colour online) Profiles of the vorticity r.m.s.: (*a*,*b*) vertical component and (*c*,*d*) horizontal component. (*a*,*c*) Cases NsD and FsD (Dirichlet, or constant buoyancy) and (*b*,*d*) cases NsN and FsN (Neumann, or constant buoyancy flux): dashed line, early time $t_1^+ \simeq 50$; solid line, final time $t_2^+ \simeq 120$.

with B_s and κ. It is also observed that the influence of the boundary conditions in the vertical component $\omega_{z,rms}$ penetrates into the overlap region slightly deeper than in the horizontal one. This behaviour is opposite to that of the velocity (see figure 11), but it is consistent with it because vertical velocity fluctuations are related to horizontal rotational motions, by definition.

One prominent difference, however, between the vorticity and the velocity is that the former approaches isotropy towards the end of the inner region: $\omega_{1,rms}^+ = \omega_{2,rms}^+ \simeq \omega_{z,rms}^+ \simeq 0.45$–$0.50$ at $z^+ \simeq 100$. The velocity field, on the other hand, is strongly anisotropic there: $w_{rms}/v_{1,rms} \simeq 1.7$–$1.8$ (see figure 11, or figure 5 at $z/z_* \simeq 0.4$).

The vorticity field becomes conspicuously anisotropic near the wall. In the case of a free-slip configuration, the vertical component in figure 12(*a*,*b*) remains relatively large all across the diffusive wall layer, as anticipated before while discussing figure 8 in § 3.4. The flat character of those profiles has been also documented by Schumacher (2009). This component of the vorticity vector has its source in the jet-like horizontal velocities along the convergence lines inside that near-wall region (Shishkina & Wagner 2008) and it is therefore consistent with higher values of $v_{1,rms}$. The horizontal component $\omega_{1,rms}^+$, on the other hand, falls to zero at the surface, by definition. This behaviour is reversed with no-slip walls, where the vertical component is forced to be zero at the surface. As expected, the no-slip condition constitutes in this case an intense source of horizontal vorticity, as reflected in figure 12(*c*,*d*).

To conclude, the temporal evolution in figure 12 provides a measure of the degree to which the inviscid scaling of the viscous dissipation rate ε is achieved in our
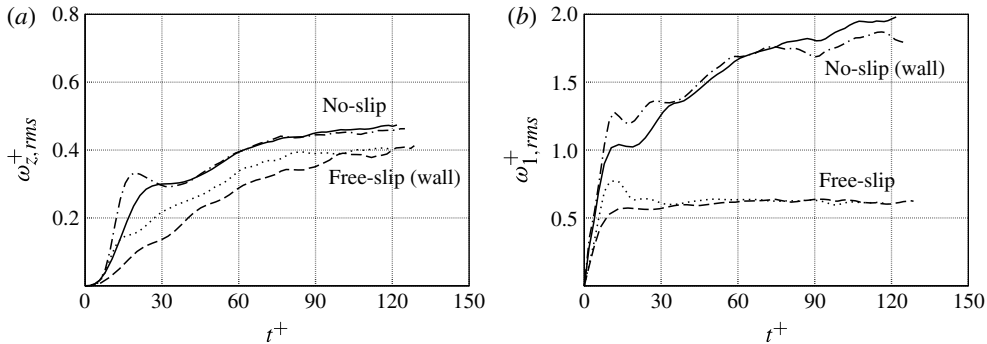
FIGURE 13. Temporal evolution of the vorticity r.m.s.: (*a*) vertical component and (*b*) horizontal component: solid line, case NsD; dashed line, case FsD; dot-dashed line, case NsN; dotted line, case FsN. In (*a*), no-slip cases correspond to the maximum in figure 12(*a*,*b*), whereas free-slip cases indicate wall values. In (*b*), no-slip cases correspond to wall values, whereas free-slip cases correspond to the maximum in figure 12(*c*,*d*).

simulations because of the relation $\varepsilon/\nu \simeq \omega^2_{rms} = \omega^2_{z,rms} + 2\omega^2_{1,rms}$. The integral form of this property has already been discussed in terms of the parameter c_ε in §3.2 and we consider it here locally, at each height. The previous relation follows from the identity $\varepsilon/(2\nu) = \omega^2_{rms}/2 + \partial^2(w^2_{rms})/\partial z^2$ and the scaling $\partial^2(w^2_{rms})/\partial z^2 \simeq w^2_*/z^2_* = (B_s z_*)^{2/3}/z^2_* = (z^2_*/B_s)^{-2/3}$, which shows that this last term becomes vanishingly small as the boundary layer broadens. The inviscid scaling $\varepsilon \simeq w^3_*/z_* = B_s$ then implies that the vorticity r.m.s. becomes steady or quasi-steady, since the surface flux B_s is steady or quasi-steady itself.

Figure 12(*c*,*d*) confirms this prediction for the horizontal components inside the overlap or inertial region, beyond 10 wall units approximately. On the other hand, the variation in the vertical component r.m.s. between t_1 and t_2 is still non-negligible, but the expected tendency is displayed in figure 13, which plots the continuous temporal evolution of ω_{rms} at some significant locations. This figure also indicates that wall values seem to approach an asymptotic behaviour as well, despite the viscosity being important there, although larger simulations are needed to be conclusive. Last, it is noted that this tendency of the magnitude of the vorticity fluctuation towards a steady state is not in contradiction with the continuous increase in the magnitude of the velocity fluctuations, but simply restates the description of the evolution of the flow included at the end of §3.1: as the boundary layer grows and the integral scales of the system increase, the small-scale characteristics, such as the diffusive sublayer and the Kolmogorov length, remain the same.

4. Conclusions

Direct numerical simulations of temporally evolving free convection over a heated plate have been presented, to the author's knowledge, for the first time. This unbounded, unsteady configuration complements previous work in buoyancy-driven systems, such as Rayleigh–Bénard convection or the convective boundary layer, which are bounded and steady, or quasi-steady. Free- and no-slip velocity conditions at the surface have been studied, for both constant buoyancy and constant buoyancy flux at the wall.

The first of the three main results concerns the vertical structure. The fine, layered structure of convection has been reproduced and, in addition, the defining heights of the different zones have been provided. The system develops an outer and inner layer, both broadening in time. The outer layer is defined by the molecular buoyancy flux being negligible compared to the turbulent flux $\langle b'w' \rangle$. This layer approaches a temporally evolving, self-preserving state characterized by the surface buoyancy flux B_s and the convection length $z_* = (1/B_s) \int_0^\infty \langle b'w' \rangle \, \mathrm{d}z$. The molecular diffusivity κ drops out of this outer (Deardorff) scaling and profiles become a function of the normalized height z/z_* only. On the other hand, the inner layer is defined by a quasi-steady behaviour in which the surface flux B_s is balanced by the turbulent transport of outer, less buoyant fluid into that region. The convection length $z_*(t)$, or equivalently the time t, drops out of the inner (Townsend) scaling, which is then based on $\{B_s, \kappa\}$, and normalized statistics inside that region depend solely on $z^+ = z \left(B_s/\kappa^3 \right)^{1/4}$ (the Prandtl number is one). The outer layer is found beyond $z^+ \simeq 10$, i.e. beyond approximately 10 wall units. The inner layer extends up to $\sim 0.4 z_*$, which means 120 wall units at the final time of our simulations, when $z_*^+ \simeq 300$.

Inside the overlap region between the inner and outer layers, the scaling based on $\{B_s, z\}$, as proposed in the classical similarity theory, is observed in the buoyancy fluctuation. The power law $b_{rms}^+ \simeq (z^+)^{-1/3}$ obtained in the simulations agrees within $10 - 20\%$ with measurements in atmospheric flows close to that local, free-convection regime. We have shown that the existence of an overlap region is a prerequisite for this power law to emerge, which occurs approximately for $z_*^+ \simeq 200$–300. This requirement corresponds to a minimum Rayleigh number $Ra \simeq 10^8$–10^9 and explains, at least in part, that this scaling has not been clearly observed in convection cells for lower Rayleigh numbers. Unlike b_{rms}, the mean gradient and the vertical velocity variance have not yet developed the expected power law, although numerical values inside that overlap region are relatively close to measurements. The data do not support either of the alternative scalings proposed in the literature. One possible interpretation of this result is that even higher Rayleigh numbers are needed for the behaviour of these quantities to become well defined; another plausible explanation is that these properties are more sensitive to outer-scale variables, as argued below.

The second major finding is the analogy in inner-region statistics between the heated plate and Rayleigh–Bénard convection. For instance, typical values of the compensated Nusselt number $Nu_* Ra_*^{-1/3}$ between 0.06 and 0.07 for $Ra_* \simeq 5 \times 10^7$–$10^9$ are recovered under no-slip conditions when the heated plate is interpreted as half a convection cell. Likewise, the thickness of the diffusive sublayer measured in terms of the mean buoyancy gradient at the wall is ~ 4 wall units for no-slip conditions and ~ 3 wall units for free-slip cases, and the maximum of the buoyancy r.m.s. profile is also found at a similar height, both results in agreement with previous work on Bénard cells. Flow structures common in free convection, such as the cellular patterns at the wall and the sheet- and mushroom-like plumes in the near-wall region, are observed in the heated plate too. All these analogies give us confidence to compare and transfer knowledge between steady and unsteady convection.

Interestingly, the compensated Nusselt number also diminishes, though mildly, with increasing Rayleigh numbers, just as in Rayleigh–Bénard convection. Physically, this variation means a gentle but persistent drift in the inner-layer statistics and prevents a state of complete steadiness inside that region. In turn, because of the one-to-one relation between the time and the convection scales, this gradual shift entails that the effect of these outer convection scales penetrate all the way down to the

surface, behaviour also observed in atmospheric convection. It can be argued that this coupling between the outer and inner layers varies among properties: for instance, it is weak in the buoyancy variance – and similarity theory prevails – but it is strong in the horizontal velocity variance. Hence, large-scale circulations can be a factor as relevant as the Rayleigh number effects considered above, and further comparisons of inner-layer statistics among different aspect ratios and with different configurations, including unsteady systems like the one described in this paper, should be performed.

Third, the influence of the boundary conditions considered in this study was found to be mainly restricted to the diffusive wall layer, approximately the first 10 wall units, once the inner scaling is used to normalize the statistics. The key point is that free-slip conditions allow horizontal motion at the surface and thus the velocity and buoyancy fluctuations in that zone are stronger than with no-slip walls. This effect leads to 30 % less buoyancy difference between the surface and the overlap region in free-slip configurations. For systems with an imposed surface buoyancy flux, this modification translates into a 30 % reduction of the mean buoyancy b_s at the plate and a 30 % narrower diffusive sublayer, compared to no-slip conditions. For systems with an imposed buoyancy at the surface, free-slip conditions mean a decrease of width of $\sim$40 % in these thin, sheet-like structures next to the wall, and 60 % higher surface fluxes B_s. This last effect has substantial consequences in the global properties because, for a given height z_*, it implies stronger turbulent fluctuations across the whole boundary layer, not only inside the near-wall region, and consequently a faster growth of the boundary layer.

To conclude, we think it is worth emphasizing that, despite the moderate Rayleigh numbers, direct numerical simulations already reach sufficient scale separation to reproduce part of the atmospheric data at much higher Rayleigh numbers and bring it together with data from other buoyancy-driven systems, such as Bénard cells. The possibility of controlled conditions and the removal of uncertainties associated with any turbulence model make direct numerical simulations a very valuable tool, not only for the fundamental study of free convection, but also, from an applied perspective, to advance current models of some relevant geophysical systems.

Acknowledgements

Appendix. Sensitivity to numerical parameters

We show in this appendix that the results discussed in the paper and the conclusions drawn are independent of the parameters related to the size of the computational box, resolution requirements and details of the initial conditions.

The aspect ratio of the turbulent boundary layer, which can be defined by the ratio L_0/z_* using L_0, the horizontal size of the computational domain, and z_*, the convective length defined by (3.5), needs to be large enough for L_0 to drop out from the analysis (Bailon-Cuba *et al.* 2010). In our simulation, this aspect ratio is large in the beginning
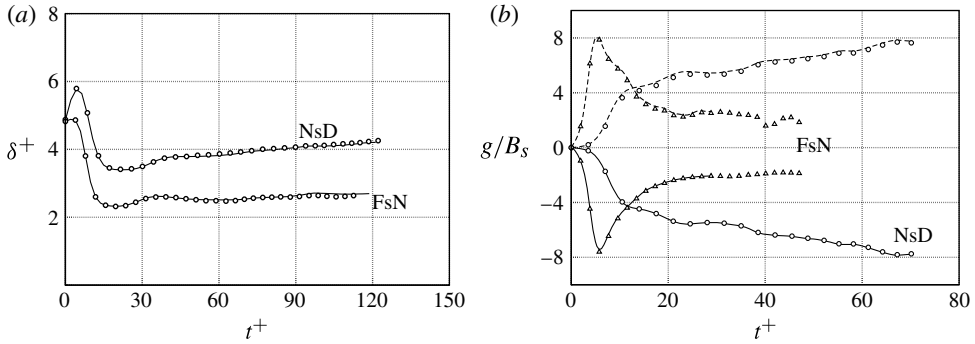
FIGURE 14. (*a*) Plot of δ, defined by (3.11): lines, the reference cases NsD and FsN, as presented in figure 7(*a*); symbols, simulations using a smaller computational box. (*b*) Resolution studies (see text), based on the budget of the turbulent kinetic energy at the rigid wall: lines, double resolution; symbols, reference resolution. Solid line, dissipation term $g = -\varepsilon$; dashed line, transport term $g = -\partial T/\partial z$.

but diminishes continuously as the boundary layer broadens in time. For all the cases in table 1, L_0/z_* is ~ 9 or larger at the time t_1 and of the order of 3 or larger at the final time t_2, and we need to ascertain if that is large enough. This was done by comparing the reference cases NsD and FsN in table 1, of horizontal size $1.5L_0 \times 1.5L_0$, with corresponding simulations of size $L_0 \times L_0$ on a grid $2048 \times 2048 \times 1534$, keeping the rest of the parameters the same. The wall values shown in figure 7(*a*) have been used to quantify the possible differences because of their relevance to the analysis. Figure 14(*a*) shows that those differences are negligible, less than 1 % for case NsD, and less than 3 % for case FsN. The major influence of L_0 for the range of aspect ratios considered here is restricted to the outer part of the outer layer, beyond the maximum of w_{rms} seen in figure 5(*a,b*), where the external intermittency is significant and the number of flow structures contained in the domain is not large enough for a good statistical convergence (see figure 1).

The effect of the vertical extension of the computational domain also needs to be addressed, since the turbulent convection layer broadens upwards in time and the simulation should be stopped when the top boundary starts to be felt by the flow. This is evaluated by monitoring the pressure r.m.s. at the top of the domain. Values ~ 3 % or less than those inside the turbulent zone are observed at the final time t_2, when the height of the computational domain is $\sim 2.8z_*$ (approximately 800 wall units). For these levels of pressure r.m.s., comparison between a reference case and a second simulation with a 20 % higher computational box shows no difference at all in the statistics investigated in this paper.

The resolution requirement is more delicate because of the importance of the diffusive layer adjacent to the wall. As part of the preliminary work, we considered a reference case on a grid $1024 \times 1024 \times 768$ and repeated the same simulation with double the resolution, that is, on a grid $2048 \times 2048 \times 1536$. We explored the cases of no-slip boundary conditions with a constant buoyancy at the wall (NsD) and free-slip with a constant buoyancy flux (FsN). We used the reference Rayleigh numbers $Ra_0 = b_0 L_0^3/(\nu\kappa)9 \times 10^8$ and $Ra_0 = B_0 L_0^4/(\nu\kappa^2) = 8.5 \times 10^{10}$, respectively (smaller than those used for the set of simulations in table 1, described in §2, to allow for a one-to-one comparison between low- and high-resolution cases).

Differences in the gradient thickness δ (not shown) are again small, less than 2 %. Mean and r.m.s. profiles are also practically indistinguishable between the two simulations, and differences are to be sought in higher-order statistics. Figure 14(*b*) plots the viscous dissipation rate ε and the divergence of the turbulent transport flux of turbulent kinetic energy at the wall. These two quantities are the only non-zero terms in the right-hand size of the budget equation of the turbulent kinetic energy at $z = 0$. With no-slip boundary conditions, case NsD, the main difference develops in the divergence $\partial T / \partial z$, with a relative error of $\sim 2 \%$ after the maximum during the transient – the error in the dissipation rate is below 0.5 %. With free-slip boundary conditions, case FsN, the error in the transport term is $\sim 5 \%$, the error in the dissipation rate $\sim 1 \%$. This accuracy corresponds to $\delta / \Delta z \simeq 6$, where δ is defined in (3.11) and Δz is the grid spacing. In terms of the Kolmogorov length $\eta = (\nu^3 / \varepsilon)^{1/4}$ at the wall, where the dissipation rate ε is maximal, the grid spacing is $\eta / \Delta z \simeq 1$ in the configuration NsD and $\eta / \Delta z \simeq 1.9$ in the case FsN (no-slip walls lead to stronger dissipation rates in the self-preserving regime, as seen in figure 14*b*). These studies, along with the scalings of the diffusive layer discussed in the paper, allow us to estimate, for a given grid size, the maximum reference Rayleigh number Ra_0 that still guarantees a good enough resolution of the small scales. In particular, $\delta / \Delta z \geqslant 6$ in all the simulations used in this work.

Last, the influence of the initial conditions on the statistics discussed in the paper was verified to be negligible. For that purpose, we performed a simulation similar to the case FsN on a grid $2048 \times 2048 \times 1536$ but with a different spectrum of $\zeta(x_1, x_2)$ of the initial perturbation. In particular, we specified it to be proportional to $(f\lambda)^2 \exp(-2f\lambda)$ instead of Gaussian, f being the spatial frequency, and with half the value of λ used in the main simulations so as to distribute more energy into the smaller scales (see § 2). In terms of δ, results show that the evolution of the system is indeed different during the initial transient, but the effect is less than 1 % beyond $t_1^+ \simeq 50$.

REFERENCES

ADRIAN, R. J. 1996 Variations of temperature and velocity fluctuations in turbulent thermal convection over horizontal surfaces. *Intl J. Heat Mass Transfer* **11**, 2303–2310.

AHLERS, G., GROSSMANN, S. & LOHSE, D. 2009 Heat transfer and large scale dynamics in turbulent Rayleigh–Bénard convection. *Rev. Mod. Phys.* **81**, 503–537.

ASAEDA, T. & WATANABE, K. 1989 The mechanism of heat transport in thermal convection at high Rayleigh numbers. *Phys. Fluids* A **1** (5), 861–867.

BAILON-CUBA, J., EMRAN, M. S. & SCHUMACHER, J. 2010 Aspect ratio dependence of heat transfer and large-scale flow in turbulent convection. *J. Fluid Mech.* **665**, 152–173.

BELJAARS, A. C. M. 1994 The parametrization of surface fluxes in large-scale models under free convection. *Q. J. R. Meteorol. Soc.* **121**, 255–270.

BELMONTE, A., TILGNER, A. & LIBCHABER, A. 1994 Temperature and velocity boundary layers in turbulent convection. *Phys. Rev.* E **50**, 269–279.

BUSINGER, J. A. 1973 A note on free convection. *Boundary-Layer Meteorol.* **4**, 323–326.

BUSINGER, J. A., WYNGAARD, J. C., IZUMI, Y. & BRADLEY, E. F. 1971 Flux-profile relationships in the atmospheric surface layer. *J. Atmos. Sci.* **28**, 181–189.

CASTAIGN, B., GUNARATNE, G., HESLOT, F., KADANOFF, L., LIBCHABER, A., THOMAE, S., WU, X. Z., ZALESKI, S. & ZANETTI, G. 1989 Scaling of hard thermal turbulence in Rayleigh–Bénard convection. *J. Fluid Mech.* **204**, 1–30.

DEARDORFF, J. W. 1970 Convective velocity and temperature scales for the unstable planetary boundary layer and for Rayleigh convection. *J. Atmos. Sci.* **27**, 1211–1213.

DEARDORFF, J. W. 1980 Cloud top entrainment instability. *J. Atmos. Sci.* **37**, 131–147.

DEARDORFF, J. W., WILLIS, G. E. & STOCKTON, B. H. 1980 Laboratory studies of the entrainment zone of a convectively mixed layer. *J. Fluid Mech.* **100**, 41–64.

ECKHARDT, B., GROSSMANN, S. & LOHSE, D. 2000 Scaling global momentum transport in Taylor–Couette and pipe flow. *Eur. Phys. J.* B **18**, 541–544.

ECKHARDT, B., GROSSMANN, S. & LOHSE, D. 2007 Fluxes and energy dissipation in thermal convection and shear flows. *Europhys. Lett.* **78**, 24001.

EMANUEL, K. A. 1994 *Atmospheric Convection*. Oxford University Press.

FEDOROVICH, E., CONZEMIUS, R. & MIRONOV, D. 2004 Convective entrainment into a shear-free linearly stratified atmosphere: bulk models reevaluated through large-eddy simulation. *J. Atmos. Sci.* **61**, 281–295.

FEDOROVICH, E. & SHAPIRO, A. 2009 Turbulent natural convection along a vertical plane immersed in a stably stratified medium. *J. Fluid Mech.* **636**, 41–57.

FERNANDES, R. L. J. & ADRIAN, R. J. 2002 Scaling of velocity and temperature fluctuations in turbulent thermal convection. *Exp. Therm. Fluid Sci.* **26**, 355–360.

FERNANDO, H. J. S. & LITTLE, L. J. 1990 Molecular-diffusive effects in penetrative convection. *Phys. Fluids* A **2**, 1592–1596.

FLACK, K. A., SAYLOR, J. R. & SMITH, G. B. 2001 Near-surface turbulence for evaporative convection at an air/water interface. *Phys. Fluids* **13** (11), 3338–3345.

GARRATT, J. R. 1992 *The Atmospheric Boundary Layer*. Cambridge University Press.

GRACHEV, A. A., FAIRALL, C. W. & BRADLEY, E. F. 2000 Convective profile constants revisited. *Boundary-Layer Meteorol.* **94**, 495–515.

GROSSMANN, S. & LOHSE, D. 2000 Scaling in thermal convection: a unifying view. *J. Fluid Mech.* **407**, 27–56.

HE, X., FUNFSCHILLING, D., NOBACH, H., BODENSCHATZ, E. & AHLERS, G. 2012 Transition to the ultimate state of turbulent Rayleigh–Bénard convection. *Phys. Rev. Lett.* **108**, 024502.

HUNT, J. C. R., VRIELING, A. J., NIEUWSTADT, F. T. M. & FERNANDO, H. J. S. 2003 The influence of the thermal diffusivity of the lower boundary on eddy motion in convection. *J. Fluid Mech.* **491**, 183–205.

JIMENEZ, J. 2012 Cascades in wall-bounded turbulence. *Annu. Rev. Fluid Mech.* **44**, 27–45.

JOHNSTON, H. & DOERING, C. R. 2009 Comparison of turbulent thermal convection between conditions of constant temperature and constant flux. *Phys. Rev. Lett.* **102**, 064501.

JULIEN, K., LEGG, S. & MCWILLIAMS, J. 1996 Rapidly rotating turbulent Rayleigh–Bénard convection. *J. Fluid Mech.* **322**, 243–273.

KATSAROS, K. B., LIU, W. T., BUSINGER, J. A. & TILLMAN, J. E. 1977 Heat transport and thermal structure in the interfacial boundary layer measured in an open tank of water in turbulent free convection. *J. Fluid Mech.* **83**, 311–335.

KRAUS, E. B. & BUSINGER, J. A. 1994 *Atmosphere–Ocean Interaction*. Oxford University Press.

LEIGHTON, R. I., SMITH, G. B. & HANDLER, R. A. 2003 Direct numerical simulation of free convection beneath an air–water interface at low Rayleigh numbers. *Phys. Fluids* **15** (10), 3181–3193.

LOHSE, D. & XIA, K.-Q. 2010 Small-scale properties of turbulent Rayleigh–Bénard convection. *Annu. Rev. Fluid Mech.* **42**, 335–364.

LUI, S.-L. & XIA, K.-Q. 1998 Spatial structure of the thermal boundary layer in turbulent convection. *Phys. Rev.* E **57** (5), 5494–5503.

MAYSTRENKO, A., RESAGK, C. & THESS, A. 2007 Structure of the thermal boundary layer for turbulent Rayleigh–Bénard convection of air in a long rectangular enclosure. *Phys. Rev.* E **75**, 066303.

MELLADO, J. P. 2010 The evaporatively driven cloud-top mixing layer. *J. Fluid Mech.* **660**, 1–32.

MELLADO, J. P. & ANSORGE, C. 2012 Factorization of the Fourier transform of the pressure-Poisson equation using finite differences in colocated grids. *Z. Angew. Math. Mech.* **92**, 380–392.

MONIN, A. S. & YAGLOM, A. M. 2007 *Statistical Fluid Mechanics,* vol. I. *Mechanics of Turbulence*, Dover.

OBUKHOV, A. M. 1946 Turbulence in an atmosphere with a non-uniform temperature. *Tr. Inst. Teo. Geofiz. Akad. Nauk. SSSR* **1**, 95–115, in Russian. English translation: *Boundary-Layer Meteorol.* (1971) **2**, 7–29.

PANOSFKY, H. A. & DUTTON, J. A. 1984 *Atmospheric Turbulence*. Wiley.

PANOFSKY, H. A., TENNEKES, H., LENSCHOW, D. H. & WYNGAARD, J. C. 1977 The characteristics of turbulent velocity components in the surface layer under convective conditions. *Boundary-Layer Meteorol.* **11**, 355–361.

POPE, S. B. 2000 *Turbulent Flows*. Cambridge University Press.

PRANDTL, L. 1932 Meteorologische Anwendung der Strömungslehre. *Beitr. Phys. Atmos.* **19**, 188–202.

PRIESTLEY, C. H. B. 1954 Convection from a large horizontal surface. *Austral. J. Phys.* **7**, 176–201.

DU PUITS, R., RESAGK, C., TILGNER, A., BUSSE, F. H. & THESS, A. 2007 Structure of thermal boundary layers in turbulent Rayleigh–Bénard convection. *J. Fluid Mech.* **572**, 231–254.

REEUWIJK, M., JONKER, H. J. J. & HANJALIĆ, K. 2008a Wind and boundary layers in Rayleigh–Bénard convection. Part 1. Analysis and modeling. *Phys. Rev.* E **77**, 036311.

REEUWIJK, M., JONKER, H. J. J. & HANJALIĆ, K. 2008b Wind and boundary layers in Rayleigh–Bénard convection. Part 2. Boundary layer character and scaling. *Phys. Rev.* E **77**, 036312.

SCHMITZ, S. & TILGNER, A. 2009 Heat transport in rotating convection without Ekman layers. *Phys. Rev.* E **80**, 015305(R).

SCHMITZ, S. & TILGNER, A. 2010 Transitions in turbulent rotating Rayleigh–Bénard convection. *Geophys. Astrophys. Fluid Dyn.* **104**, 481–489.

SCHUMACHER, J. 2008 Lagrangian dispersion and heat transport in convective turbulence. *Phys. Rev. Lett.* **100**, 134502.

SCHUMACHER, J. 2009 Lagrangian studies in convective turbulence. *Phys. Rev.* E **79**, 056301.

SHISHKINA, O. & WAGNER, C. 2006 Analysis of thermal dissipation rates in turbulent Rayleigh–Bénard convection. *J. Fluid Mech.* **546**, 51–60.

SHISHKINA, O. & WAGNER, C. 2008 Analysis of sheet-like thermal plumes in turbulent Rayleigh–Bénard convection. *J. Fluid Mech.* **599**, 383–404.

SIGGIA, E. D. 1994 High Rayleigh number convection. *Annu. Rev. Fluid Mech.* **26**, 137–168.

SORBJAN, Z. 1996 Comments on 'A convective transport theory for surface fluxes'. *J. Atmos. Sci.* **54**, 576–578.

STEVENS, B. 2005 Atmospheric moist convection. *Annu. Rev. Earth Planet. Sci.* **33**, 605–643.

STEVENS, R. J. A. M, LOHSE, D. & VERZICCO, R. 2011 Prandtl and Rayleigh number dependence of heat transport in high Rayleigh number thermal convection. *J. Fluid Mech.* **688**, 31–43.

STEVENS, R. J. A. M, VERZICCO, R. & LOHSE, D. 2010 Radial boundary layer structure and Nusselt number in Rayleigh–Bénard convection. *J. Fluid Mech.* **643**, 495–507.

STULL, R. B. 1988 *An Introduction to Boundary Layer Meteorology*. Kluwer Academic.

SULLIVAN, P. P. & PATTON, E. G. 2011 The effect of mesh resolution on convective boundary layer statistics and structures generated by large-eddy simulations. *J. Atmos. Sci.* **68**, 2395–2415.

TENNEKES, H. & DRIEDONKS, A. G. M. 1981 Basic entrainment equations for the atmospheric boundary layer. *Boundary-Layer Meteorol.* **20**, 515–531.

TENNEKES, H. & LUMLEY, J. L. 1972 *A First Course in Turbulence*. MIT Press.

THEERTHAN, S. A. & ARAKERI, J. H. 2000 Planform structure and heat transfer in turbulent free convection over horizontal surfaces. *Phys. Fluids* **12** (4), 884–894.

TOWNSEND, A. A. 1959 Temperature fluctuations over a heated horizontal surface. *J. Fluid Mech.* **5**, 209–241.

TURNER, J. S. 1973 *Buoyancy Effects in Fluids*. Cambridge University Press.

VERZICCO, R. 2004 Effects of nonperfect thermal sources in turbulent thermal convection. *Phys. Fluids* **16**, 1965–1979.

VERZICCO, R. & SREENIVASAN, K. R. 2008 A comparison of turbulent thermal convection between conditions of constant temperature and constant heat flux. *J. Fluid Mech.* **595**, 203–219.

WEIDAUER, T., PAULUIS, O. & SCHUMACHER, J. 2010 Cloud patterns and mixing properties in shallow moist Rayleigh–Bénard convection. *New J. Phys.* **12**, 105002.

WILLIS, G. E. & DEARDORFF, J. W. 1974 A laboratory model of the unstable planetary boundary layer. *J. Atmos. Sci.* **31**, 1297–1307.

WYNGAARD, J. C. 2010 *Turbulence in the Atmosphere*. Cambridge University Press.

WYNGAARD, J. C., COTÉ, O. R. & IZUMI, Y. 1971 Local free convection, similarity, and the budget of shear stress and heat flux. *J. Atmos. Sci.* **28**, 1171–1182.

ZHOU, Q., SUN, C. & XIA, K.-Q. 2007 Morphological evolution of thermal plumes in turbulent Rayleigh–Bénard convection. *Phys. Rev. Lett.* **98**, 074501.

ZILITINKEVICH, S. S. 1991. *Turbulent Penetrative Convection*. Avebury Technical.